

Microphysical Perturbation Experiments and Ensemble Forecasts on Summertime Heavy Rainfall over Northern Taiwan

JEN-PING CHEN,^{a,b,c} TZU-CHIN TSAI,^a MIN-DUAN TZENG,^a CHI-SHUIN LIAO,^a HUNG-CHI KUO,^a
AND JING-SHAN HONG^d

^a *Department of Atmospheric Sciences, National Taiwan University, Taipei, Taiwan*

^b *International Degree Program in Climate Change and Sustainable Development, National Taiwan University, Taipei, Taiwan*

^c *Research Center for Environmental Changes, Academia Sinica, Taipei, Taiwan*

^d *Central Weather Bureau, Taipei, Taiwan*

(Manuscript received 20 October 2021, in final form 26 May 2022)

ABSTRACT: Microphysical perturbation experiments were conducted to investigate the sensitivity of convective heavy rain simulation to cloud microphysical parameterization and its feasibility for ensemble forecasts. An ensemble of 20 perturbation members differing in either the microphysics package or process treatments within a single scheme was applied to simulate 10 summer-afternoon heavy-rain convection cases. The simulations revealed substantial disagreements in the location and amplitude of peak rainfall among the microphysics-package and single-scheme members, with an overall spread of 57%–161%, 66%–161%, and 65%–149% of the observed average rainfall, maximum rainfall, and maximum intensity, respectively. The single-scheme members revealed that the simulation of heavy convective precipitation is quite sensitive to factors including ice-particle fall speed parameterization, aerosol type, ice particle shape, and size distribution representation. The microphysical ensemble can derive reasonable probability of occurrence for a location-specific heavy-rain forecast. Spatial-forecast performance indices up to 0.6 were attained by applying an optimal fuzzy radius of about 8 km for the warning-area coverage. The forecasts tend to be more successful for more organized convection. Spectral mapping methods were further applied to provide ensemble forecasts for the 10 heavy rainfall cases. For most cases, realistic spatial patterns were derived with spatial correlation up to 0.8. The quantitative performance in average rainfall, maximum rainfall, and maximum intensity from the ensembles reached correlations of 0.83, 0.84, and 0.51, respectively, with the observed values.

SIGNIFICANCE STATEMENT: Heavy rainfall from summer convections is stochastic in terms of intensity and location; therefore, an accurate deterministic forecast is often challenging. We designed perturbation experiments to explore weather forecasting models' sensitivity to cloud microphysical parameterizations and the feasibility of application to ensemble forecast. Promising results were obtained from simulations of 10 real cases. The cloud microphysical ensemble approach may provide reasonable forecasts of heavy rainfall probability and convincing rainfall spatial distribution, particularly for more organized convection.

KEYWORDS: Cloud microphysics; Ensembles; Cloud parameterizations; Mesoscale models

1. Introduction

Heavy convective precipitation may cause disasters such as flooding and landslides; therefore, it is an essential subject for weather forecasting and disaster management. The development of summer convective rainfall depends not only on environmental forcing but also on in-cloud microphysical processes (Andreae et al. 2004; Rosenfeld et al. 2008; Tao et al. 2012), which, in turn, influence cloud dynamics through latent heating/cooling, precipitation drag, cold pool formation, and cloud radiation. Together, these factors determine rainfall's intensity, timing, and location, factors critical to the issue of disaster warning. However, the forecast of heavy convective rain has always been challenging because of the relatively small temporal and spatial scales of convection systems, which cannot be resolved well by observations (Weckwerth 2000) or numerical simulations (Lynn et al. 2001).

Earlier studies on heavy convective precipitation forecast have relied on radiosonde-derived thermodynamic indices in

the form of a checklist for diagnosing the prospect of heavy rainfall (e.g., Showalter 1953; Jefferson 1963; Miller 1972; Andersson et al. 1989; Gordon and Albert 2000). However, studies have suggested that such indices' reliability depends on geographical location, and no single index performed well in all regions (Haklander and Delden 2003; Marinaki et al. 2006; Sanchez et al. 2001). With the advent of numerical weather prediction (NWP), heavy rainfall forecasting has shown some promise. Nonetheless, the NWP models are often inadequate in heavy rainfall's intensity and location (Junker and Hoke 1990; Nam et al. 2014; Shahrban et al. 2016; Sikder and Hossain 2016; Majumdar et al. 2021); they are also limited in providing a proper diagnosis of heavy convective rainfall in regions without sufficient observations (Birch et al. 2014; Sahlaoui et al. 2020).

One of the key factors for an accurate precipitation forecast by an NWP model is the initial conditions, which inevitably contain various uncertainties. The error associated with such uncertainties can grow upscale and significantly affect forecast accuracy (Lorenz 1969; Rotunno and Snyder 2008; Johnson et al. 2014). A way to deal with such uncertainties is to perform

Corresponding author: Jen-Ping Chen, jpchen@ntu.edu.tw

DOI: 10.1175/WAF-D-22-0004.1

© 2022 American Meteorological Society. For information regarding reuse of this content and general copyright information, consult the [AMS Copyright Policy \(www.ametsoc.org/PUBSReuseLicenses\)](#).

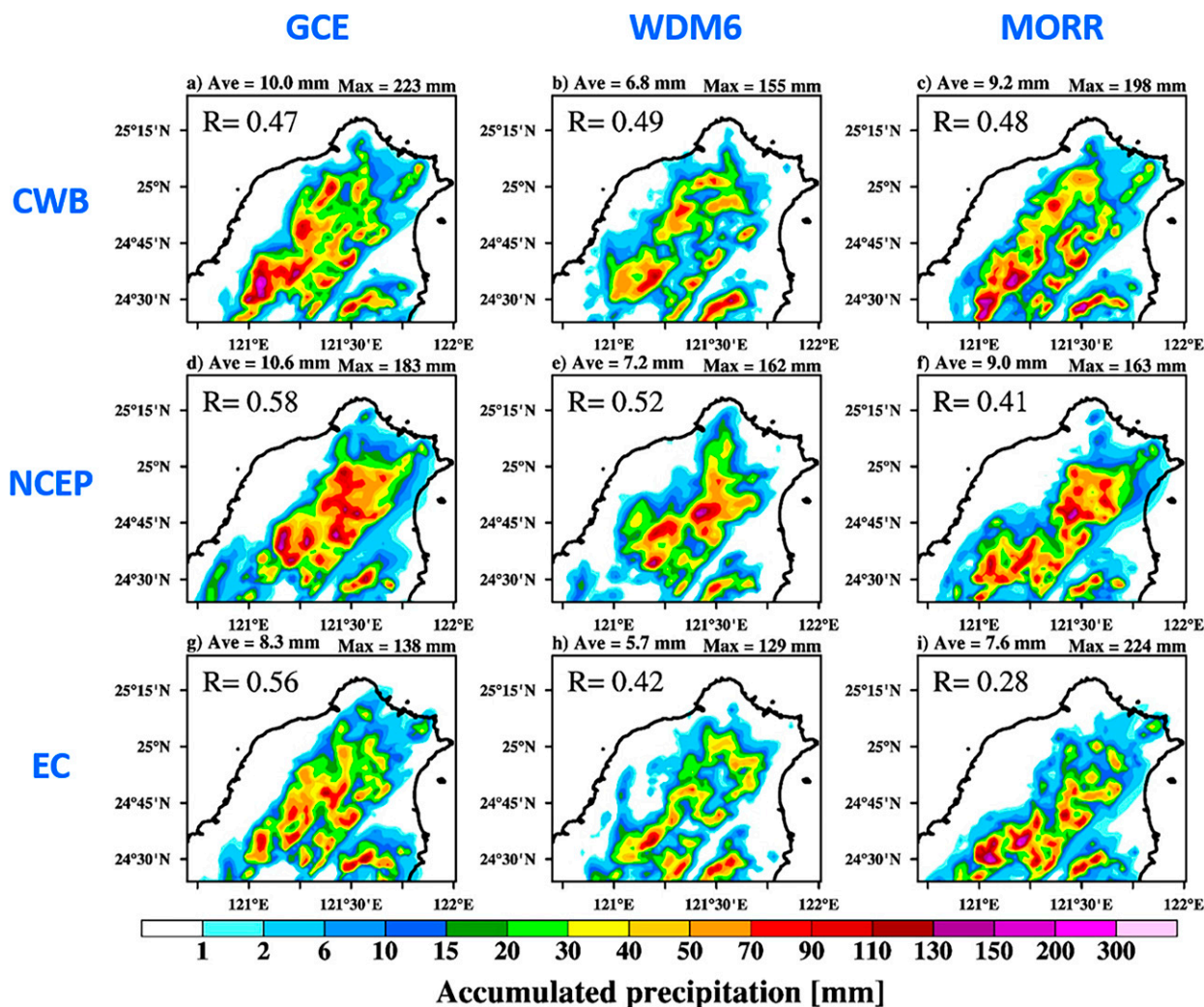


FIG. 1. Accumulated rainfall during 0000–1200 UTC 14 Jun 2015 over northern Taiwan from a summer convective system simulated with the WRF Model. The model setup is the same as described in section 2a. The rows show simulations using three different initial/boundary conditions from (a)–(c) the Global Forecast System of the Central Weather Bureau (CWB), (d)–(f) the Final Operational Global Analysis of the National Centers for Environmental Prediction (NCEP), and (g)–(i) the ERA-Interim reanalysis data from the European Centre for Medium-Range Weather Forecasts (EC). The columns show results using three different microphysics schemes: (left) GCE, (center) WDM6, and (right) MORR (details of these WRF options given in section 2b). Domain average and maximum accumulation are listed above each panel, and the spatial correlation with the QPESUMS data is listed in the top-left corner of each panel.

an ensemble forecast using perturbed initial and boundary conditions (Ehrendorfer 1997; Hohenegger et al. 2008; Kühnlein et al. 2014; Keresturi et al. 2019). Other than the initial and boundary conditions, NWP models also contain uncertainties in the physics parameterization schemes. Some NWP centers have applied a multimodel approach to address uncertainties in both the physics and dynamics, such as the THORPEX Interactive Grand Global Ensemble (Bougeault et al. 2010), the North American Ensemble Forecast System (Candille et al. 2010), and the NCEP Short-Range Ensemble Forecast system (Du et al. 2003). Multiphysics in a single model is another approach that focuses on the uncertainties in individual physics schemes (Du et al. 2003; García-Díez et al. 2015; Jankov et al. 2017). Such approaches have the advantage of potential bias

cancelation that leads to an improved ensemble forecast and produces a good ensemble spread (Duan et al. 2012). The ensemble technique may be particularly beneficial for convective-scale NWP because of the convective systems' fast evolution and chaotic nature. The short predictability time scales caused a new scale of uncertainty that did not exist in the lower resolution models (WMO 2012).

However, it is costly for a single NWP center to maintain and develop multiple models or physics schemes. It is also unaffordable to sample the full range of uncertainty in convective precipitation with huge ensembles. Identifying the largest uncertainties in the model may help reduce the number of ensemble members and optimize ensemble forecasts. Figure 1 demonstrates the diversity in heavy rain simulation when

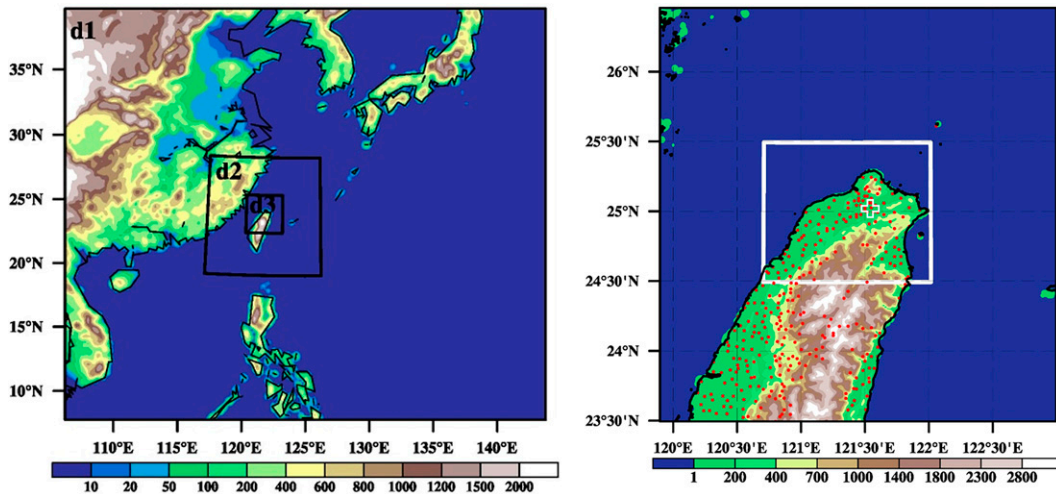


FIG. 2. Settings of the model domains. (left) Layout of first (d1), second (d2), and third (d3) domains, with horizontal grid spacings of 20, 4, and 1.33 km, respectively. (right) A zoom-up of domain 3, with rain gauge locations indicated by red dots. The white-rectangular box in domain 3 is the focal area for later analysis, with the “+” sign indicating the Taipei City center. The color scale represents the terrain height (m).

applying different initial and boundary conditions (IBC) or cloud microphysical parameterizations (CMP) for a case to be discussed further in section 3. One can see that perturbation in both IBC and CMP introduced significant discrepancies among simulations. However, the CMP perturbations disagree more among themselves compared to the IBC perturbations. The mean of normalized standard deviation (standard deviation divided by the average) in average rainfall and maximum rainfall among the CMP perturbations are 66% and 12%, respectively, higher than those among the IBC perturbations. Also, the spatial correlations against the observational data are less similar among the CMP than the IBC perturbations. Although we used only a minimum number of perturbations for this example, the results suggest that uncertainties in CMP are no less significant than those in IBC for convective rainfall simulations. Toth and Kalnay (1997) indicated that successful ensemble forecasts require all significant error sources to be considered in the ensemble design. Therefore, considering CMP uncertainties could be critical to ensemble forecast, at least for predicting heavy rainfall from summer convection.

Purely physical perturbation ensembles are rare in operational forecasts. However, the influence of cloud microphysical parameterizations has been investigated widely (cf. Morrison et al. 2020). For example, Fovell et al. (2009) found a significant impact of cloud microphysics schemes on the track of an idealized hurricane. Qiao et al. (2018) demonstrated the effect of perturbed temperature tendency for microphysical processes and hydrometeor size distribution in an idealized supercell simulation. In a real-case ensemble forecast experiment, Wang et al. (2020) found that stochastically perturbing the hydrometeor terminal velocities according to their error characteristics can better match the observation than symmetrical perturbations for convective precipitation forecast. With observational guidance, Stanford et al. (2019) stochastically varied the coefficients of the ice particle mass-size and fall speed-size relationships; they

found significant effects on cloud radiation and precipitation. Gaudet et al. (2021) conducted a comprehensive investigation by applying different microphysics schemes and perturbing individual processes for a snowstorm precipitation forecast. They found that even though the position of the snowfall is relatively consistent among the CMP members, the intensity of snowfall varied significantly. All these studies demonstrated the sensitivity of modeled cloud and precipitation to microphysical parameterization.

This study aims to identify critical microphysical uncertainties and investigate the potential of the microphysical ensemble for heavy-rain probability forecast. The Taipei metropolis is selected as the focal area because of its high population density (nearly 7 million in a basin of about 90-km² size) and relatively frequent flood-causing convective rainfall during the summer (Akaeda et al. 1995; Chen et al. 2007; Chen et al. 2009; Lin et al. 2011). Furthermore, the Taipei metropolis is located in a basin surrounded by hills and mountains with two river valleys funneling streams and airflow (cf. Fig. 2). The complicated interactions between the land–sea-breeze effect, heat island effect, and complex orography make the heavy-rain objective forecast particularly challenging for this area (Lin et al. 2012). Therefore, we performed multimember simulations on 10 summertime heavy-rain events to discuss the uncertainties in microphysical parameterization, and the potential of using CMP perturbations for ensemble forecasting of convective rainfall. We also evaluated the performance of the CMP ensemble for heavy-rain intensity and location forecasts.

The remainder of the paper is organized as follows. Section 2 describes the heavy-rainfall cases selected for simulation and the model setup, including the selection of perturbation members. Section 3 discusses the perturbation experiment results, with details from a demonstration case and the statistics from all 10 cases. How the perturbation experiment can be applied to ensemble forecasts, including the heavy-rain probability

TABLE 1. List of selected summer heavy rainfall cases around the Taipei Metropolis and their rainfall characteristics. The “#” and “@” signs respectively indicate rain gauge and QPESUM data provided by the Central Weather Bureau.

Date	No. of stations with heavy rain [#]	Max intensity [#] (mm h ⁻¹)	Max 3-h accumulation [#] (mm)	Max intensity [@] (mm h ⁻¹)	Max 24-h accumulation [@] (mm)	Avg rainfall [@] (mm)
23 Jun 2013	8	69.5	119.5	69.3	119.8	8.9
6 Jul 2013	8	97.5	130.5	100.5	138.8	6.2
25 Jul 2013	4	55.5	100.0	57.5	113.0	3.8
23 Jun 2014	12	91.0	179.0	91.3	254.0	17.7
29 Jun 2014	5	59.5	78.0	55.5	113.0	14.0
14 Jun 2015	6	105.0	187.5	80.3	205.0	7.2
23 Jul 2015	5	64.0	80.5	111.8	152.0	9.0
18 Aug 2015	7	70.5	124.0	107.5	199.8	13.9
17 Jun 2016	8	79.0	140.0	148.3	341.0	18.3
29 Jun 2016	6	71.5	104.0	94.5	208.5	17.6

distribution and intensity forecast, is presented in section 4. The final section gives a summary and conclusions.

2. Methodology

a. Case selection and model setup

The heavy-rainfall threshold adopted here for case selection is hourly intensity $> 40 \text{ mm h}^{-1}$ or 3-h accumulation $> 100 \text{ mm}$ based on measurements from around 110 automatic rain gauges (cf. Fig. 2b). We ignored events with possible influence from nearby (within 300 km) weather systems (such as typhoons or cold fronts) and weak events with less than three sites reaching the heavy-rain threshold. A total of 10 summer-afternoon heavy precipitation cases (see Table 1) occurred during 2013–16 over the Taipei Metropolis and its surroundings fit the criteria and thus were selected. The 14 June 2015 event is designated as the demonstration case (hereafter named case 150614), with a more detailed microphysical analysis given in section 3. Note that, in the studied area, heavy rainfall often occurred over the mountainside, where rain gauge stations are scarce. Therefore, a different rainfall dataset from the “quantitative precipitation estimation and segregation using multiple sensors” (QPESUMS; Chang et al. 2021) provided by the Central Weather Bureau is used for obtaining regional rainfall statistics in later analyses because of its better spatial coverage. This QPESUMS system assimilates observations from multiple mixed-band weather radars and rain gauges, as well as NWP model results, to produce 1-km resolution intensity every 10 min.

The numerical model selected for this study is the Weather Research and Forecasting (WRF) Model version 3.8.1 (Skamarock et al. 2008), which provides a suite of cloud microphysical schemes that are suitable for our purpose. The simulations applied three two-way-nesting domains (cf. Fig. 2) with horizontal grid spacings of 20, 4, and 1.33 km, respectively, and each contains 210×180 , 251×251 and 241×241 grids. Our discussions focus on results in the central region of the inner domain, which covered the whole northern Taiwan with the Taipei Metropolis located to the north (cf. Fig. 2). In the vertical dimension, 45 sigma layers were used. The ERA-Interim reanalysis data from the European Centre for Medium-Range Weather Forecasts (EC-ERA) were used for the initial and

boundary conditions. For each case, the simulations started at 2000 local time (1200 UTC) on the previous day for sufficient model spinup. The analyses start from 0800 local time to midnight. For the studied afternoon thunderstorm cases, convective clouds and precipitation generally developed in the late morning. Therefore, the effective spinup time is more than 12 h, in accordance with the recommendation by Jankov et al. (2007). Also, the rainfall accumulated in the analyzed period is equivalent to a daily accumulation. The physics options applied include the Kain–Fritsch cumulus scheme (Kain 2004; used only for the first domain), YSU planetary boundary layer scheme (Hong et al. 2006), Goddard Space Flight Center radiation scheme (Matsui et al. 2018), Noah Land Surface Model (Tewari et al. 2004), and revised MM5 surface layer scheme (Jimenez et al. 2012). Several cloud microphysics schemes are selected to form the ensemble members, with details described as follows.

b. Microphysics schemes and perturbation members

A total of nine different microphysical schemes (members 1–9; hereafter called the MS members) in the WRF model were chosen as CMP members (cf. Table 2). In addition, we also perturbed physical processes and size-distribution representations that have been shown to significantly influence the performance of cloud microphysical parameterization (Morrison et al. 2020). These perturbations (members 10–24; hereafter called the NTU members) are variations from the NTU scheme (Tsai and Chen 2020), which was chosen because of its comprehensiveness in treating microphysical processes and its use of up to three predicted moments to resolve the size distributions. Because the focus of this study is the perturbation and ensemble techniques, we avoid judging individual members’ performance in later discussions. Note that the simulation for case 160616 using the MY2 scheme was not successful for unknown numerical problems and thus was excluded from later analyses.

The mathematical representations addressed here focus on the hydrometeors’ size distribution, which is conventionally described with a gamma-type function as follows:

$$n(D) = N_0 D^\alpha \exp(-\lambda D), \quad (1)$$

where D is the diameter; and N_0 , α , and λ are the size-distribution parameters called the intercept, spectral dispersion, and slope,

TABLE 2. List of microphysical perturbation members. In the setup descriptions, 1M, 2M, and 3M (or when not specified) denote one-moment, two-moment, and three-moment schemes, respectively. In the code names for the NTU scheme, α represent the “shape factor” in the gamma-type size distribution in Eq. (1); the suffix “S” indicates spherical shape; “V” indicates empirical fall speed (power-law dependence on size; independent of shape and density); “C” or “P” represent clean or polluted aerosol types, respectively; “L” or “H” indicate lower (1/100 times) or higher (100 times) ice nuclei (IN) concentrations; “T” indicates “traditional” parameterization setups (i.e., empirical fall speed, spherical ice-phase hydrometeors); “ R_i ” indicates the i th simulation with randomized collision efficiency for ice–liquid and ice–ice interactions; and “ I_i ” indicates the i th simulation with randomized initial conditions. The WRF options refer to those in versions 3.8.1 if not specified.

Member No.	Microphysics scheme	Member code	Descriptions	Reference(s)
1	Lin	LIN	1M; option 2 in WRF	Chen and Sun (2002)
2	GCE	GCE	1M; option 7 in WRF	Tao et al. (1989, 2016)
3	WSM6	WSM6	1M; option 6 in WRF	Hong and Lim (2006)
4	WDM6	WDM6	Semi-2M, option 16 in WRF	Lim and Hong (2010)
5	MORR	MORR	Semi-2M, option 10 in WRF	Morrison et al. (2009)
6	MY2	MY2	2M, option 9 in WRF	Milbrandt and Yau (2005b)
7	NSSL	NSSL-1M	1M; option 19 in WRF	
8		NSSL-2M	2M, option 18 in WRF	Mansell et al. (2010)
9	NTU	NTU	Default (3M; continental background aerosol); option 56 in WRF version 4.3 or later	Tsai and Chen (2020)
10		NTU-C	Maritime (clean) aerosol	
11		NTU-P	Urban (polluted) aerosol	
12		NTU-L	Low IN concentration	
13		NTU-H	High IN concentration	
14		NTU- V_R	Power-law fall speed for raindrops	
15		NTU- V_I	Power-law fall speed for ice-phase hydrometeors	
16		NTU-S	Spherical ice crystal	
17		NTU- $2\alpha_d$	2M, diagnosed α for ice-phase hydrometeors	
18		NTU- $2\alpha_f$	2M, fixed α (=3 for pristine ice and =0 for other ice-phase hydrometeors)	
19		NTU-2S	2M, $\alpha = 0$ and spherical shape for all ice-phase hydrometeors	
20		NTU-2T	Same as NTU-2S, but with power-law fall speed for all hydrometeors (“T” stands for traditional)	
21–24		NTU- R_0 –NTU- R_3	Default + randomized collision efficiency	
25–28		NTU- I_0 –NTU- I_3	Default + randomized initial conditions	

respectively. Studies have shown that how we select and describe the spectral parameters in Eq. (1) has a strong influence on model results (Milbrandt and Yau 2005a,b; Morrison et al. 2009; Tsai and Chen 2020; Milbrandt et al. 2021). The cloud model usually tracks the moments (or their derivative variables) of the size distribution, which is expressed as the following:

$$M_j = \int D^j n(D) dD, \tag{2}$$

where j is the order of moment. Among the perturbation members shown in Table 1, members 1–3 and 7 (LIN, WSM6, GCE, and NSSL-1M) are single moment (1M) schemes, which keep track of the mixing ratio of each hydrometeor category (correspond to the third moment, M_3 , when divided by the specified particle density). For such schemes, only one of the three size-distribution parameters in Eq. (1) can be derived, and λ usually is selected to vary with M_3 while N_0 and α are kept constant (the latter traditionally set to zero). Members 4–6 and 8 (i.e., WDM6, MORR, MY2, and NSSL-2M) are either partially (for selected hydrometeor categories) or fully double

moment (2M) schemes that track an additional parameter—the number mixing ratio (equivalent to M_0). However, α still needs to be either specified as a constant or diagnosed from other parameters. The NTU triple moment (3M) scheme (members 9–16 and 21–24) further tracks the second moment (M_2 ; proportional to the surface area) so that α becomes a predictive variable. We also utilize the 2M version of the NTU scheme, which applied diagnosed or fixed α (members 17–20).

Besides the size distribution functions, uncertainties also exist in the description of physical processes. This study takes the NTU scheme (member 9) as the default setting and perturbs individual processes in subsequent members. Members 10–11 tested the aerosol effect on cloud drop formation by switching the types (size distributions) of condensation nuclei from the default “continental background” to either “maritime” (clean) or “urban” (polluted) types (cf. Whitby 1978). Ice nuclei (IN) concentration used in the default setting is 400 L^{-1} according to Georgii and Kleinjung (1967) and Chen and Lamb (1994), which is also approximately a medium value in the global simulation of Hoose et al. (2010) for nondesert areas. Members 12–13 alter the default ice nuclei concentration

by 0.01 or 100 times. Members 14–15 applied simplified (power-law type, similar to that in the Morrison scheme) fall speed parameterization for raindrops and ice-phase hydrometeors, respectively. By contrast, the default NTU scheme applied raindrop group fall speed parameterized from bin-model results (Chen and Liu 2004) and ice-particle fall speed from Mitchell and Heymsfield (2005), which considered the particle shape and density effects (cf. Tsai and Chen 2020). Member 16 assumes all ice particles are spherical (as done in most traditional schemes) in contrast to the variable-shape approach in the default setup (cf. Tsai and Chen 2020), in which the shape factor affects the vapor deposition, collision, and sedimentation processes of pristine ice crystals and snow aggregates. Among the four NTU 2M schemes, member 17 applied a pseudo3M method for ice-phase hydrometeors, in which α is diagnosed (similar to Milbrandt and Yau 2005a,b) using empirical formulas derived from NTU-3M simulations; member 18 applied $\alpha = 3$ for the pristine ice crystals (cf. Chen and Tsai 2016) and $\alpha = 0$ for other ice-phase hydrometeors; member 19 mixes two simplifications: 2M with $\alpha = 0$ (the conventional approach) and spherical ice particles; whereas member 20 further applied the power-law type fall speeds for all hydrometeors.

The above members' selection takes into consideration critical microphysical factors identified in earlier studies, such as fall speed (e.g., Tsai and Chen 2020; Milbrandt et al. 2021), condensation nuclei and ice nuclei (e.g., Teller and Levin 2006; Kuba and Fujiyoshi 2006; Fan et al. 2017; Keita et al. 2020), ice crystal shape (e.g., Harrington et al. 2013; Chen and Tsai 2016; Tsai and Chen 2020), and size distribution representations (e.g., Milbrandt and Yau 2005a,b; Morrison et al. 2009; Tsai and Chen 2020). Another consideration is uncertainty in the collection efficiency for hydrodynamic interactions between hydrometeors. The parameterization of liquid-phase particle interactions in the NTU scheme follows the statistical–physical method of Chen and Liu (2004), which implicitly included the realistic variations of collection efficiency documented in the literature. However, the collection efficiencies for the ice–ice or ice–liquid collision processes are highly simplified. Because of a lack of more advanced parameterizations, the NTU scheme assumed that the collection efficiency is either a constant or a simple function of interacting particle masses, as done in most current schemes. To touch upon its uncertainty, we adopted a random perturbation approach by multiplying the collection efficiency with a random number between 0.5 and 2.0 at each grid and every time steps; this treatment is repeated four times (members 21–24) with different number sequences. Four additional tests (members 25–28) were applied using random perturbations to the initial low-level potential temperature field to contrast microphysical perturbations and initial-condition perturbations. Following Stanford et al. (2019), the perturbations were applied using a random-number generator to create a Gaussian distribution with a standard deviation of ± 0.1 K. Due to their simplicity and relatively low impact, we only mentioned members 21–28 in the main-case discussion and exclude them in the ensemble probability analysis.

3. Microphysical perturbations

a. Rainfall intensity and spatial patterns for case 150614

We first demonstrate the large discrepancies in simulated heavy rainfall among different members using case 14 June 2015 (150614). This case is a severe afternoon thunderstorm system that developed under a weak southwesterly monsoon background. It produced the highest maximum intensity (105 mm h^{-1}) and 3-h accumulation (187.5 mm) among the 10 selected events according to the rain gauge data (but not QPESUMS). Even though the interaction between dynamic and thermodynamic mechanisms for this event is interesting (Miao and Yang 2020), this study will focus on only its microphysical aspects.

Figure 3 shows a comparison of the spatial distribution of the 24-h accumulation. Most members roughly caught the overall spatial pattern exhibited by either the rain gauge or QPESUMS data. However, many also produced heavier rain from the southern convection cell instead of the northern cell shown in the observation. The spatial correlation coefficients compared to the QPESUMS data range from 0.39 (NTU-V) to 0.65 (NTU- V_R), indicating significant variation in spatial patterns. Figure 3 also indicates that the spatial-pattern variation is relatively large among the NTU members. A contrasting result was obtained by Gaudet et al. (2021), who applied a similar suit of microphysical perturbation members to simulate an Ontario lake-effect snowstorm. They found greater consistency in spatial patterns among the NTU members than MS members.

Interestingly, rainfall from the group with the randomized collection efficiency (members 21–24; figures not shown) produced spatial patterns quite similar to that of NTU (member 9) but fluctuated noticeably in the maximum intensity and accumulation (see Fig. 4). As the randomization was executed every time step, the average collection efficiency from members 9 and 21–24 should be quite similar after a few hours of simulation. Nonetheless, the maximum intensity or accumulation still differed appreciably among these members, indicating that the collection process is nonlinear and the subsequent microphysical chain reactions may be chaotic. However, likely due to other controlling factors (such as forcing from orography and background flow), such a perturbation does not significantly influence rainfall's spatial pattern for case 150614. The variations due to the initial-condition perturbations (members 25–28) are even smaller than the randomized collection efficiency, supporting the results in Fig. 1. A word of caution, though; the spread from initial-condition perturbations may vary with the microphysical scheme (Wang et al. 2012; Chen et al. 2021), an issue not explored in this study.

The simulated maximum accumulation also varied greatly, from the least of 52 mm (NTU-V) to the highest of 313 mm (NSSL-1M). Nevertheless, these values well enclose that from the surface rain gauges (189 mm) or QPESUMS (205 mm). Note that the maximum accumulation and intensity may depend on the grid resolution. Nevertheless, the inconsistency should be small because the model resolution (1.33 km) is close to the QPESUMS resolution (1 km). Eight members (WSM6, GCE, MORR, MY2, NTU-H, NTU- $2\alpha_d$, NTU- R_0 ,

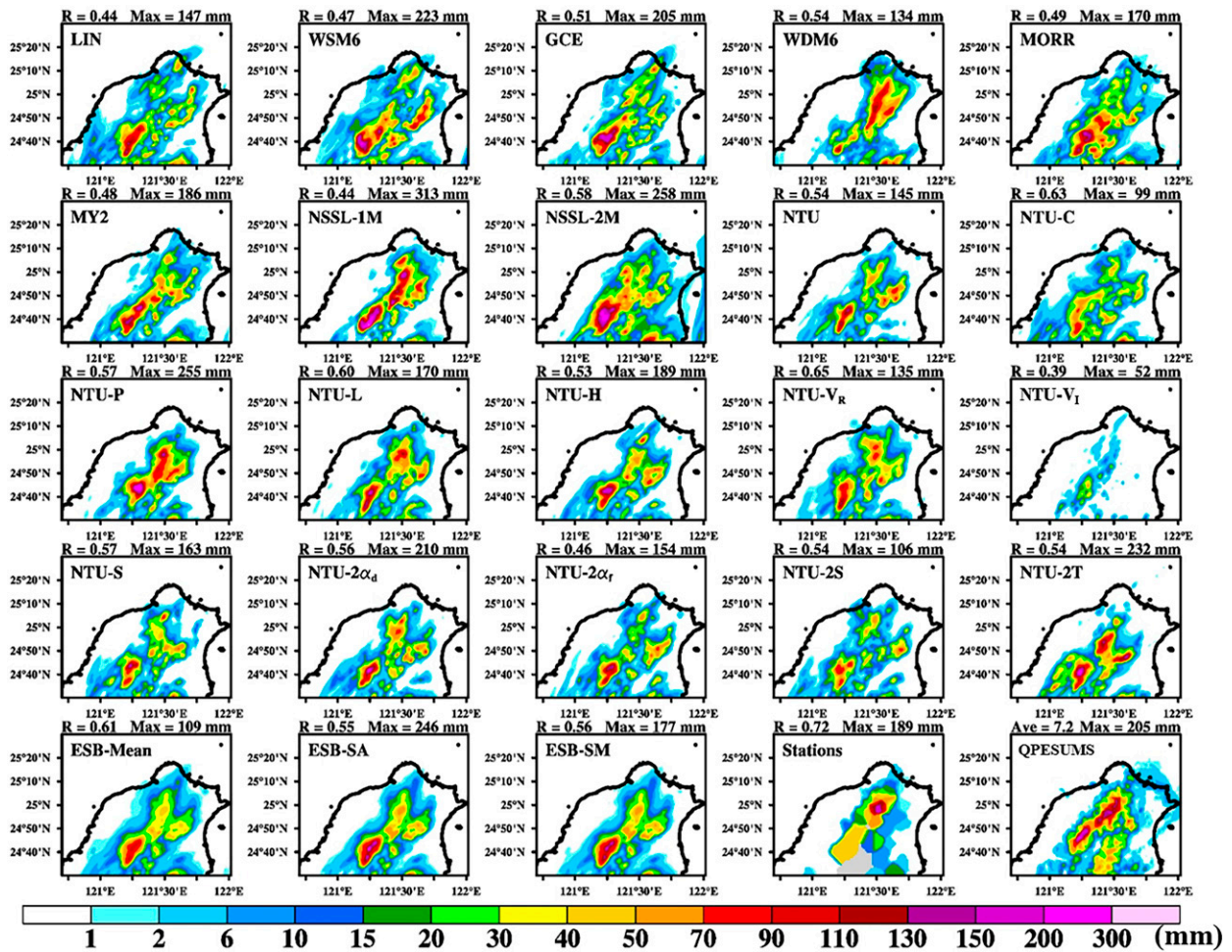


FIG. 3. The simulated and observed daily cumulative rainfall for case 150614. The top four rows are simulations with the perturbation members 1–20 that are listed in Table 2. Panels in the last row from left to right, respectively, are the results from the simple ensemble mean (ESB_Mean), the “sort-all” spectral mapping (ESB_SA), the “sort-within-member” spectral mapping (ESB_SM), the cubic spline interpolation of rain gauge observations, and the 1-km resolution QPESUMS data. The color scale indicates rainfall amount (mm).

and NTU-R₃) produced peak accumulation within 10% of the rain gauge or QPESUM data. The spread of the rainfall simulation is summarized in Fig. 4. Taking the QPESUMS rainfall data as a reference, the models generally produced insufficient average 24-h rainfall (RF_{ave}) and maximum 24-h accumulation (RF_{max}) but stronger maximum intensity (RI_{max}). Significant discrepancies exist not only among different microphysics schemes (members 1–9) but also among different process treatments within the NTU scheme (members 9–24), and the latter is by no means less significant. The spread of RF_{ave} , RF_{max} , and RI_{max} among different MS members (members 1–9) is 65%, 87%, and 98%, respectively, of the observed values. Such variations are somewhat less prominent than those (69%, 99%, and 132%, respectively) among the members using different process treatments in the NTU scheme (members 9–24). The overall spreads (members 1–24) are 114%, 127%, and 150%, respectively. These spreads are somewhat more significant than those (91% and 108% at two observation sites)

for the lake-effect heavy snowfall ensemble by Gaudet et al. (2021).

The treatment of randomized collection efficiency and initial conditions caused relatively minor deviations from the default NTU scheme: approximately within 14% in RF_{ave} , 39% in RF_{max} , and 67% in RI_{max} for randomized collection efficiency, and 9% in RF_{ave} , 15% in RF_{max} , and 33% in RI_{max} . Because the randomizations in collection efficiency and initial conditions do not significantly add to the model spread, members 21–28 were excluded from the ensemble analysis in the following sections.

b. Rainfall spread statistics for 10 cases

The microphysical sensitivities illustrated above do vary substantially from case to case. Among the 10 cases, the range of spreads (in % of the observed values) in RF_{ave} , RF_{max} , and RI_{max} are 55%–161%, 59%–145%, and 42%–115% among the MS members; 17%–72%, 21%–99%, and 43%–126% for

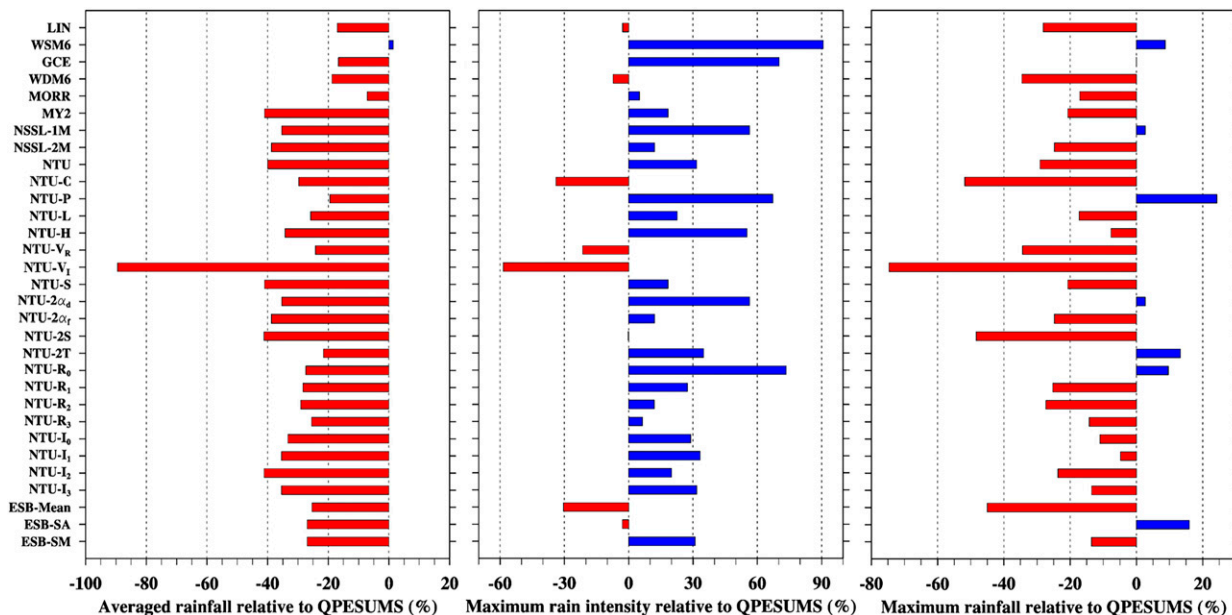


FIG. 4. Rainfall discrepancy (in %) relative to the QPESUMS data from 28 microphysical perturbation members and the ensemble methods for case 150614. (left) Average rainfall, (center) maximum accumulation, and (right) maximum intensity. The reference (observation) values are listed in Table 1.

NTU members, and 57%–161%, 66%–161%, and 65%–149% for all members. One may observe that case 150614 (Fig. 4) may not be very typical comparing to the statistics of all 10 events shown in Fig. 5. The spreads among the NTU members are mostly smaller than those among the MS members. In fact, more than half of the cases showed substantially larger standard deviations in rainfall indices among MS members than the NTU members. Such a result is understandable because the MS members differed in a suite of parameterizations, whereas the NTU members picked only a few processes/parameters for perturbation. Nevertheless, the degree of diversity among NTU members remains substantial when looking at the 10 cases as a whole.

Although some members may tend (say, more than 75% incidences) to produce higher or lower rainfall than observations, few members produced consistent biases (always positive or negative) for the 10 cases. Only two schemes (WDM6 and NTU) contained the observed values in the interquartile range of the box-and-whisker plot, which indicates their relatively small biases in the three rainfall indices (i.e., RF_{ave} , RF_{max} , and RI_{max}). Large biases can also be found in some NTU-scheme variations, including NTU-C, NTU-V, NTU- $2\alpha_r$, and NTU-2T. These indicate that the possible causes of bias in the heavy-rain simulation are the model's treatment in aerosol type, fall speed parameterization, and the spectral shape of the size distribution. Note that NTU- $2\alpha_r$ is somewhat more sophisticated than NTU- $2\alpha_d$, yet it seems to perform somewhat worse in all three rainfall indices. This result may suggest a possible cancellation of biases from different microphysical processes. On the other hand, NTU-V changed only the ice-particle fall speed, but the effect seems much more dramatic than NTU-2T, which

additionally altered the size distribution. This suggests that the traditional power-law fall speed may have been adapted for use with the traditional Marshall–Palmer distribution.

c. Hydrometeors vertical distribution

Everything else being equal, the members' disagreement on surface rainfall should result from the different treatment in microphysical processes, which can be reflected in the quantity of hydrometeors. In a microphysical perturbation experiment on lake-effect snowfall, Gaudet et al. (2021) showed that the surface precipitation type (e.g., snow, graupel, or rain) varied more strongly than the total precipitation quantity among the perturbation members. So, in the following, we briefly examine the discrepancy in hydrometeors among different perturbation members. Note that the NTU scheme applied a “pristine cloud ice” category that differs from the traditional “cloud ice” category. Such pristine cloud ice can grow by vapor deposition without a size limit and thus may be large enough to be called “snow” in conventional definition. The traditional category of snow, in turn, is redefined as snow aggregates. It helps to compare only the sum of cloud ice (pristine cloud ice) and snow (aggregates) between NTU and other schemes. Also, some microphysical schemes do not distinguish between graupel and hail; therefore, one may combine hail and graupel when comparing their quantity in different schemes.

Figure 6 shows the vertical profile of each hydrometeor's mass concentration averaged over the inner domain and the whole simulation time. The basic patterns look similar, with cloud ice, snow, graupel/hail, cloud drop, and raindrop sequentially emerging at different heights. However, substantial

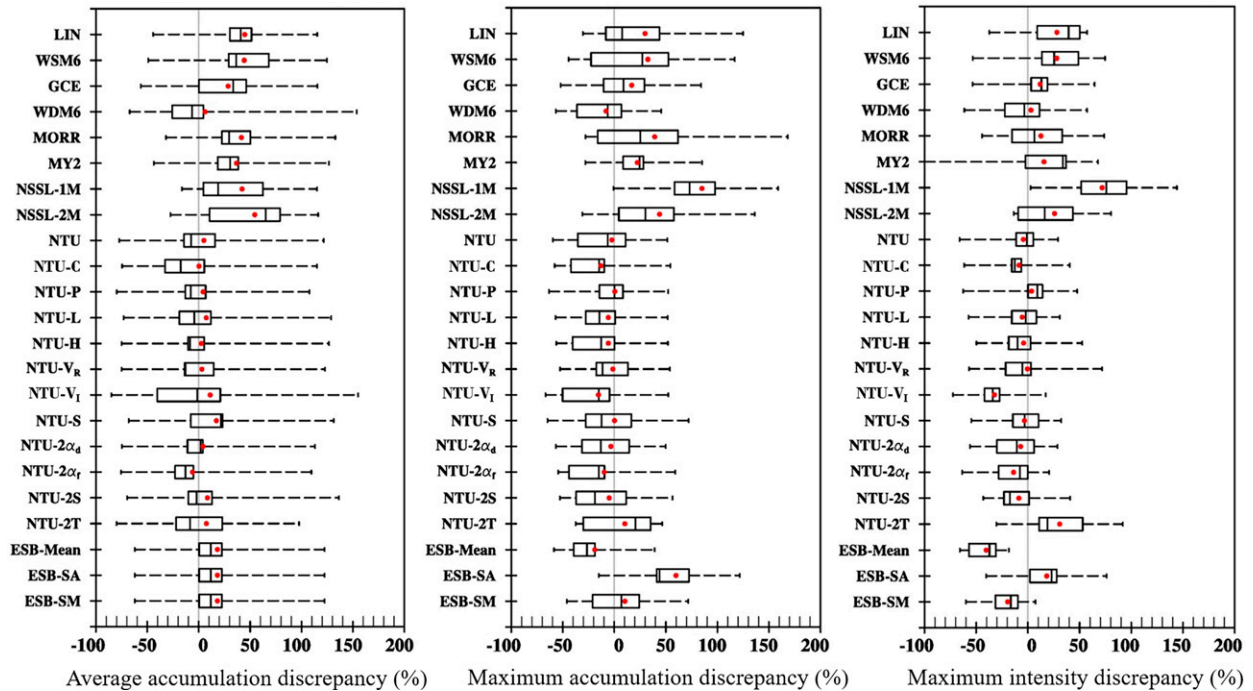


FIG. 5. As in Fig. 4, but for the 10 cases and expressed with box-and-whisker plot diagrams. The rectangular box, the vertical line within the box, and the red dot indicate the interquartile range (25%–75%), median, and mean, respectively, while the whisker ends indicate the extreme values.

diversity exists in the relative amount and the altitude where the maximum proportion occurs for each hydrometeor. The differences are most significant in ice-phase hydrometeors. Some members produced a prominent upper-level peak in total mass (e.g., WSM6, GCE, MORR, NSSL-2M, NTU-V, and NTU-2T), but the occurred heights ranged from 6 to 13 km. A few members produced more graupel than cloud ice and snow combined. The highest proportion of condensate to exist as graupel ranges from approximately 20% (NSSL-2M) to 87% (LIN). The spread in graupel’s mass fraction is smaller among the NTU members except NTU-V and NTU-2T, with the lowest of roughly 58% (NTU-R₃) to the highest of 81% (NTU-C). Substantial differences also exist among the NTU-scheme members. In particular, the member NTU-V showed much cloud ice near the cloud top but only a meager fraction of snow and graupel at all heights, which may explain its lowest rainfall amount and intensity (cf. Figs. 3 and 5). NTU-2T (in effect NTU-V plus 2M size distribution) also produced an ample amount of cloud ice aloft, indicating the ice-particle fall-speed treatment can significantly affect the growth and conversion of cloud ice to snow and graupel; however, the effect is less significant when the 2M size distribution is also applied. Furthermore, NTU-V produced significantly less cloud water and rainwater. A possible reason is that the weak production of precipitation (mainly graupel and snow) resulted in weaker dynamic feedbacks through the cold-pool mechanism, which was suggested to be a critical factor for convection development in this heavy-rain event (Miao and Yang 2020). Other microphysical processes can also contribute to

intermember discrepancies, but the details will not be elaborated further here.

4. Heavy-rain ensemble forecast

a. Location-specific heavy-rain probability

An important aspect of heavy rain forecasting is the probability of occurrence and issuing a warning for specific locations. The spatial patterns shown in Fig. 3 provide a good example of diversity in heavy-rain spatial patterns, which may be utilized for a location-specific probability forecast. Following Ebert (2001), counting the fraction of members that produced heavy rain at specific locations (grids) can yield a heavy-rain probability map, as shown in Fig. 7 for the 10 studied cases under the $>40 \text{ mm h}^{-1}$ criterion. The ensemble results produced areas of significant probability (roughly $>20\%$) at locations near the spot of actual occurrence, with heavy-rain center mostly within about 10 km distance. One exception is case 130623, where the high probability area is more than 20 km away from the actual heavy-rain zone. For the more organized convective systems (e.g., cases 140623, 150614, 150723, 150818, and 160617), the highest heavy-rain probability may reach well over 70%. The better performance for the more organized heavy-rain systems is possibly due to their distinct thermodynamic and orographic forcing. When the areas of occurrence are scattered (or less organized), the forecasted areas also tend to be patchy with greater location mismatch (e.g., cases 130623, 130706, 130725, 140629, and 160629).

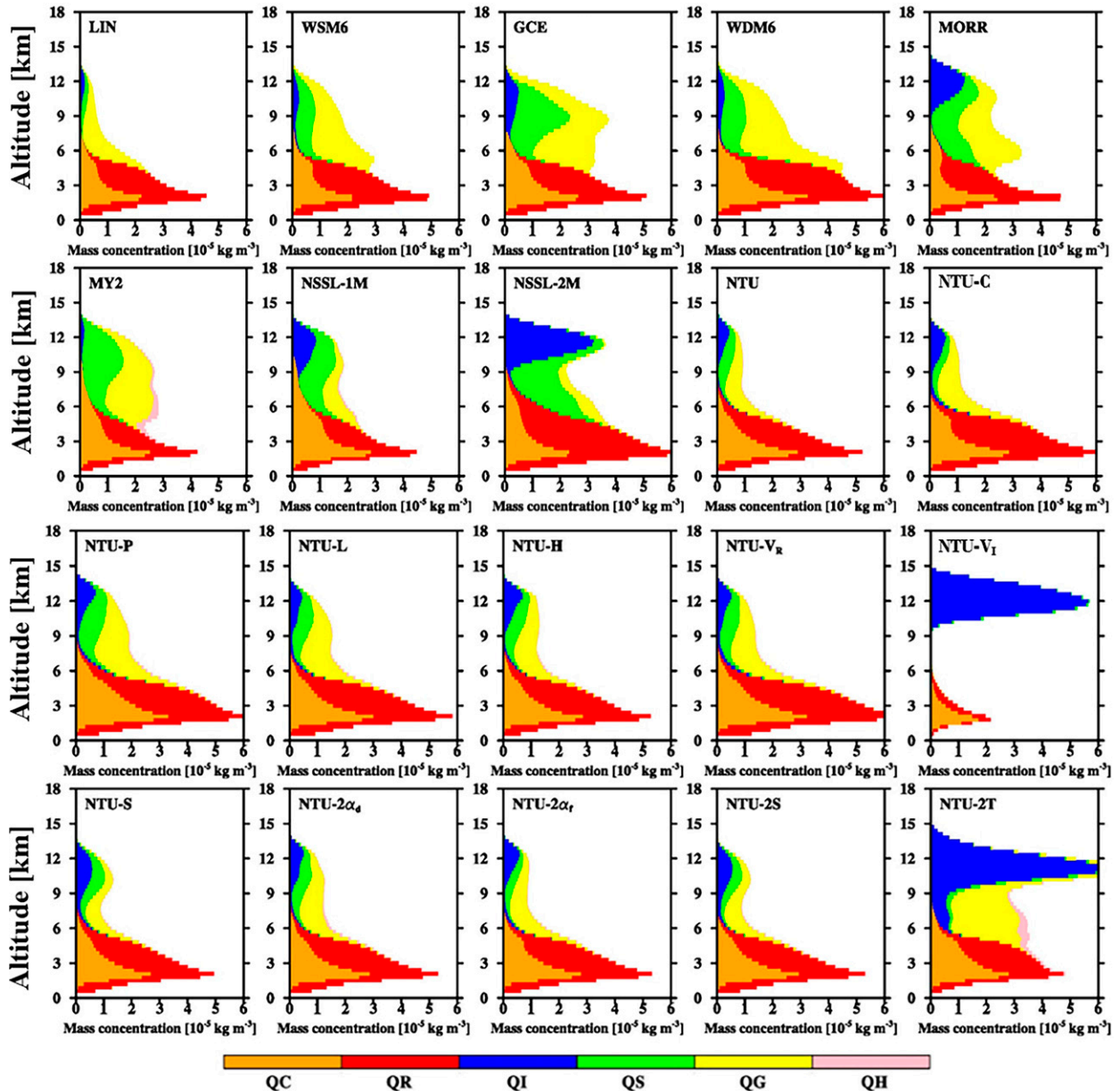


FIG. 6. Vertical profile of different hydrometeors from each microphysical perturbation member for case 150614. The abscissa shows the mass concentration ($10^{-5} \text{ kg m}^{-3}$) of each hydrometeor species averaged over the focus area (cf. Fig. 2); the ordinate shows the altitudes regridded into 1-km height intervals from original model levels. The color scheme indicates the hydrometeor species with QC, QR, QI, QS, QG, and QH representing cloud drop, raindrop, cloud ice, snow, graupel, and hail, respectively.

The above results suggest that the microphysical ensemble technique may have a decent capability in pinpointing the location of heavy rain, which is essential for disaster preparation. So, we evaluated the location correctness of heavy-rain binary (yes/no) forecasts from ensemble members by adopting two performance indices commonly applied in meteorological forecasts: the threat score (TS) and accuracy (ACY). Other performance indices may also be used but are ignored to condense the discussion. The TS index (also called the critical success index) is the ratio of

hits to all forecasted or observed “events,” defined as the following:

$$TS \equiv \frac{a}{a + b + c}, \tag{3}$$

where a is the number of members forecasted the incidents (hits), b is the number of members forecasted but not occurred in reality (false alarms), and c is the number occurred but not forecasted (misses). Terms in the denominator indicate that TS emphasizes the occurred events, whereas the ACY

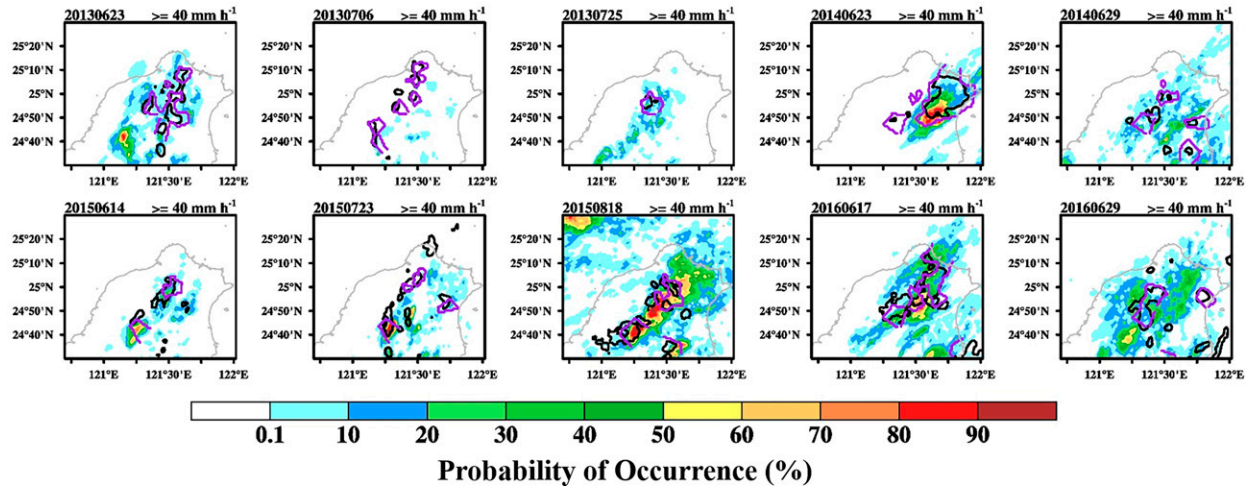


FIG. 7. Probability (in %) of hourly intensity exceeding 40 mm h^{-1} for the 10 selected cases. The color shading indicates the probability from microphysical perturbation members, and the black and purple lines indicate the areas that observed heavy rain ($>40 \text{ mm h}^{-1}$) according to the QPESUMS and rain gauge data, respectively.

index also considers the correctness of forecasting the nonevents according to the following definition:

$$\text{ACY} \equiv \frac{a + d}{a + b + c + d}, \quad (4)$$

where d is the number of observed nonevents that are forecasted correctly (correct rejects). Conventionally, these two fractional indices are used to evaluate the skill in forecasting a certain kind of event over a long period. Here, we applied them to assess the daily forecast skill at particular locations in a single rainfall incidence using statistics from different members, not various rainfall cases as in traditional usage. Therefore, false alarms cannot apply to occurred incidents (i.e., heavy rain), whereas misses cannot apply to nonevents (i.e., not heavy rain). Similarly, false alarms and misses are mutually exclusive. Thus, the contingency table collapses to a binary mask such that the conventional equitable threat score is not applicable.

A factor that needs to be considered in forecasting the heavy-rain locations is the dependence on the size of the warning area. Because it is difficult for the forecasts to pinpoint and match observations, particularly for increasingly higher model resolutions, a spatial window is often applied to provide verification at multiple scales. However, a wider warning area will increase the probability of detection [also called prefiguration = $a/(a + c)$] but, at the same time, also increase the false alarm rate [= $b/(a + b)$]. To test the spatial prediction ability of the ensemble model, we applied the fuzzy radius concept to explore the sensitivity of model performance to the size of the warning area (cf. Ebert 2008). Under this concept, a success (hit) is awarded when the forecasted event (or nonevent) is within a distance R (i.e., the fuzzy radius) of the observed event. We intend to find an optimal R that returns helpful indices for evaluating the model performance in heavy-rain spatial forecasts.

Using case 150614 as an example, Fig. 8 illustrates the performance indices' variation with R . Both the TS and ACY

indices varied significantly with increasing R in terms of spatial pattern and score values when R is below 8 km. After R reached 8 km, the spatial pattern converged with the observed heavy-rain area (cf. Fig. 7), but the scores at the “hit” areas kept on increasing until R reached about 14 km. For a pinpoint warning ($R = 0$), the TS barely reached 0.25 over a limited area. In contrast, the ACY index is similar over the observed heavy-rain area but approaches 1.0 over much of the nonevent areas. For an overprecautious warning (e.g., $R > 14$ km), TS and ACY may reach about 0.8 over the event areas, which is the fraction of members that did produce heavy rain in the inner domain, but accompanied with zero scores over a broad surrounding area.

The overall results from the 10 cases suggest that, for more (less) organized convective systems, the effective warning radius from our microphysical ensemble is about 6 (10) km, and the average is about 8 km. Figure 9 shows the spatial performance indices under $R = 8$ km for the 10 selected cases. Apparently, the ensemble results for the more organized convection cases tend to achieve higher TS scores with several locations even acquiring $\text{TS} > 0.6$. In contrast, the five less organized convection events had relatively low TS (< 0.2) due to either low hits in the heavy-rain area or false alarms in nonevent areas, whereas the size of the low ACY area is also smaller due to the limited heavy-rain occurrence.

b. Heavy-rain quantitative forecast

In principle, the results from different members can provide an ensemble mean that generally verifies better than an unperturbed (control) forecast because it smooths out the unpredictable forecast elements (WMO 2012). However, for precipitation forecast, a simple ensemble by taking area averages of different members tends to underestimate the heavy rain and overestimate the weak rainfall primarily because of a mismatch in convection's locations. For example, in the relatively better-simulated case 150614, a simple ensemble average

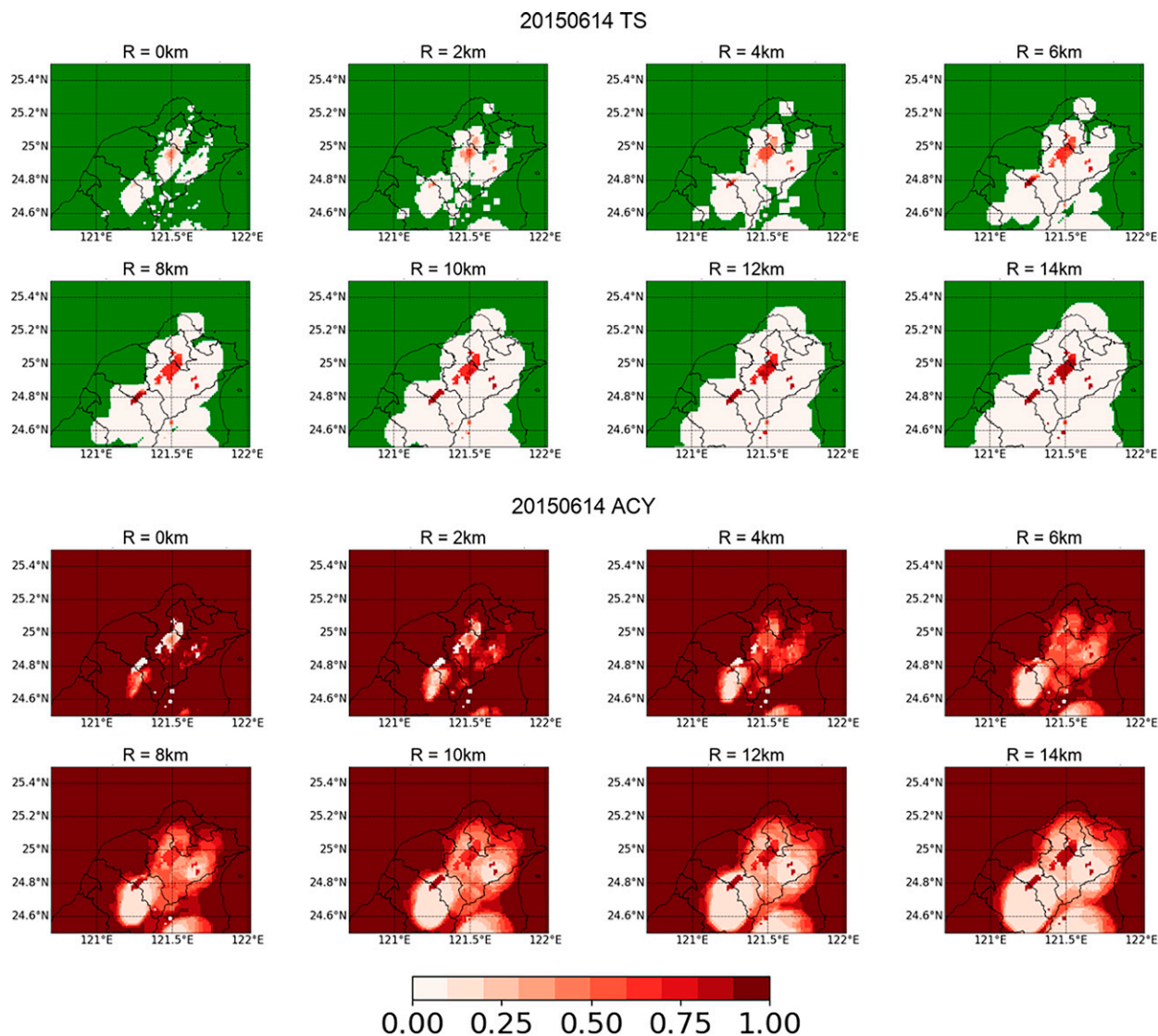


FIG. 8. Effect of warning area extent (fuzzy radius) on the performance indices for heavy rain ($>40 \text{ mm h}^{-1}$) spatial forecast for case 150614. (top) TS and (bottom) ACY. The green shaded area in the top panels indicates that no members forecasted heavy rain and thus cannot be evaluated with TS. For panels of $R = 0$, the warning location is the center of each model grid. Results for $R > 14 \text{ km}$ do not differ significantly from those with $R = 14 \text{ km}$ and thus are omitted. Color shading indicates the performance indices from 0 to 1.

would yield a peak accumulation of 113 mm (ESB_Mean in Fig. 3), which is about 67% (81%) less than the observed peak from rain gauges (QPESUMS).

A way to resolve this drawback is to apply the spectral remapping method (cf. Ebert 2001), similar to those used for synthesizing audio signal (Grey and Moorer 1977) or image downscaling (Gastal and Oliveira 2017). The rationale is that the peak values from each member may be more trustworthy than the locations. The spectral remapping method utilizes the ensemble spatial pattern to position the peak-rainfall areas while preserving the peak values from each member, and it operates in two steps. First, for an ensemble of m ($=20$ in this study) members, each with n grids (241×241 in this study) in the simulation domain, the $m \times n$ grids are first sorted according to

their rainfall amounts (either the intensity or the accumulation) and rearranged into n subsets (ranks). Then, the m values in the first rank are synthesized to yield a representative value for that rank, which is remapped to the grid of highest rainfall determined from the simple ensemble mean. The same procedure is operated sequentially on the remaining $n - 1$ sets of values.

There are various ways of synthesizing the values of the same rank to provide a representative value of that rank. In a study of precipitation ensemble forecast, Ebert (2001) suggested using the median value based on the bimodal nature of the rainfall distribution, which is either zero (the usual case) or distributed in lognormal form when rain occurs. However, in heavy rain situations, the rainfall values in a particular rank

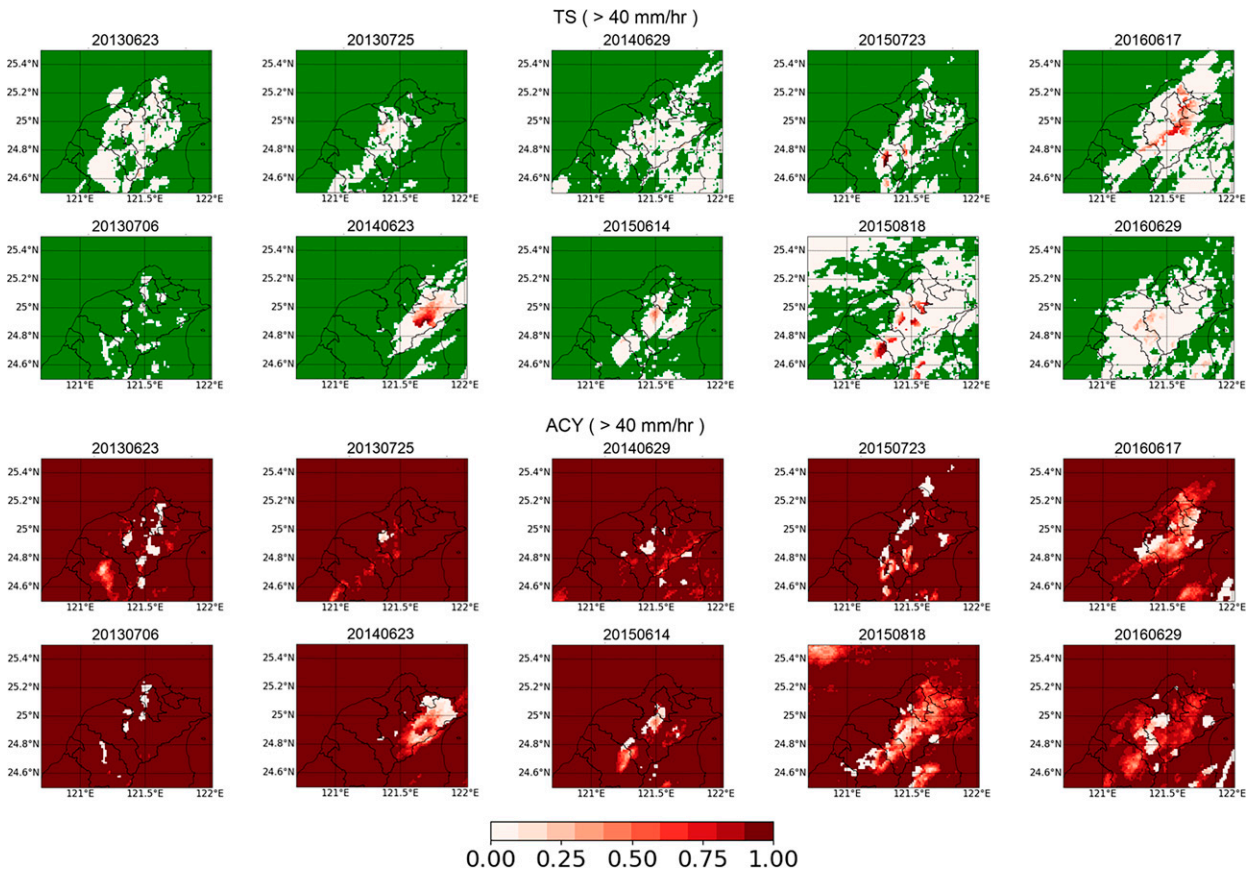


FIG. 9. As in Fig. 8, but for the 10 selected cases and with fuzzy radius $R = 8$ km.

tend to be similar due to sorting and thus are not bimodal. Another technique Ebert (2001) suggested is to apply the “majority rules” so that rain is forecasted only where more than half of the ensemble members predicted rain, and the rain rate is averaged from only those members. Yet, this method affects only the median to lower rank sets and has minimal effect on heavy rain forecast.

Therefore, a straightforward averaging of all m values of the same rank seems reasonable for our purpose, using two slightly different approaches. First, we sort the precipitation strength within each member, then average those with the same rank across the members (hereafter called SM, stands for “sort within member”). Second, we sort all grids from all members, and then take the average of each successive m number of values (can be from the same member) to yield the ensemble ranking (hereafter called SA, stands for “sort all”). For case 150614, the SM approach generated a maximum accumulation of 177 mm (cf. ESB_SM in Fig. 3), which improved significantly over the simple ensemble mean even though it is still a bit short of the observed value. In contrast, the SA approach produced a peak value of 242 mm (cf. ESB_SA in Fig. 3), which went a bit too far. Because the top-ranked values in the SA approach can be from the same member, peak heavy rain tends to bias toward a few strong members. On the other hand, the SM approach suffers from always including the weak

members. Therefore, the maximum value from ESB_SA is usually significantly higher than that from the SM approach.

Figure 10 shows rainfall’s spatial pattern derived from the spectral-mapping ensembles. The spatial correlations between ESM_SA (ESM_SM) and observation range from 0.26 (0.28) for case 130706 to 0.79 (0.80) for case 140623. Apparently, more organized events attained better matches. According to Fig. 11, the variation in spatial correlation is much more substantial among different events than among different members. The median (mean) of the spatial correlation among the 10 cases is around 0.64 (0.60) from the ensemble results, significantly higher than all individual members (median: 0.54–0.61, mean 0.53–0.58) (Fig. 11a). Furthermore, the ensemble results outperformed most (and often all) individual members for all events except case 130706 (Fig. 11b), which is the least organized and most difficult to simulate. Interestingly, the spectral mapping approach somewhat degraded the spatial correlation as can be seen from the consistently higher spatial correlation in ESB_Mean than ESM_SM and ESB_SA (Fig. 11b).

Besides the spatial pattern (location), the ensemble forecast may help determine the peak amount and intensity of heavy rainfall, also crucial information for disaster warnings. The SM and SA approach each has its strength in peak rainfall predictions. Comparing the three ensembles (ESB_Mean, ESB_SA, and ESB_SM) and individual members altogether,

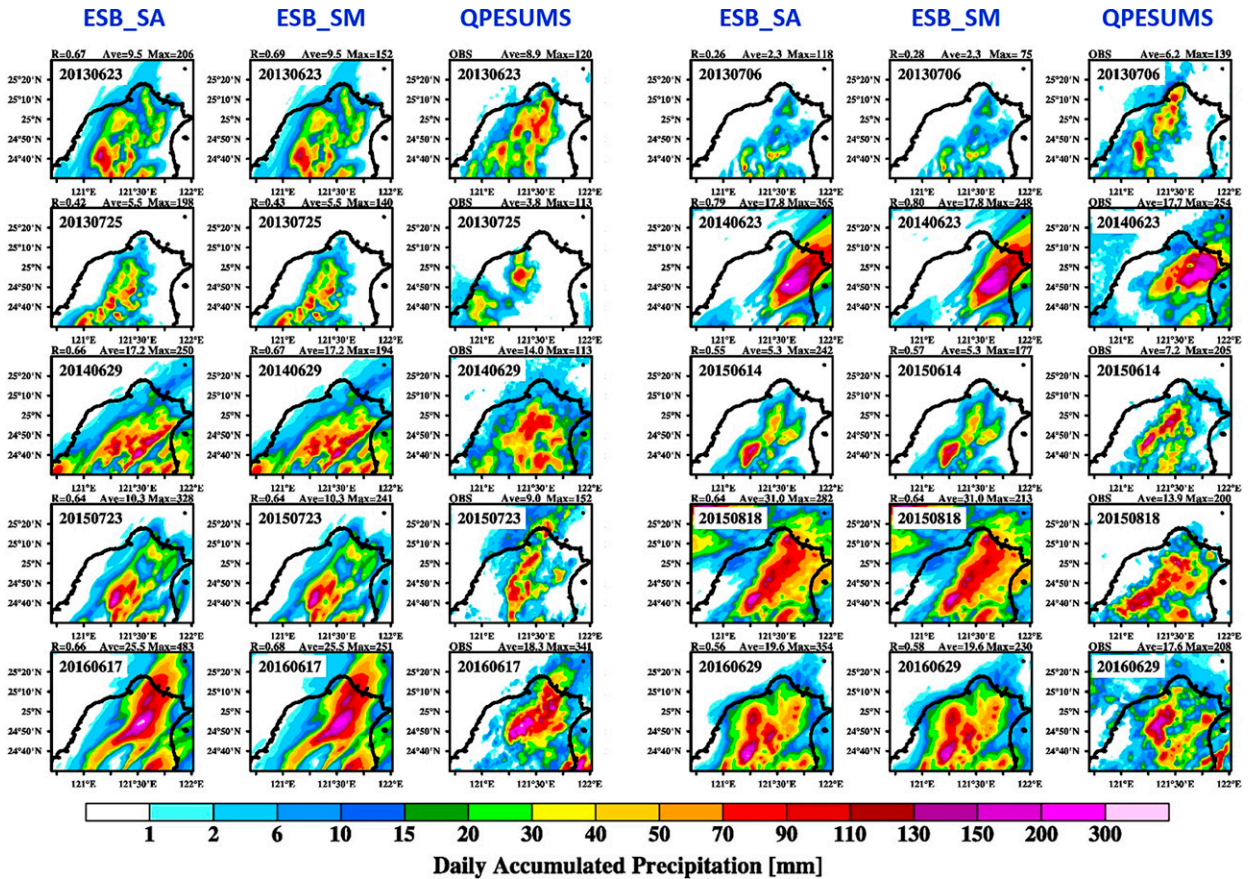


FIG. 10. Ensemble forecast of the accumulation using the spectral remapping methods for the 10 simulated events. The results from (left) ESB_SA, (center) ESB_SM, and (right) QPESUMS data. The date of each case is indicated at the top-left corner of each panel; the spatial correlation (with QPESUMS), average rainfall, and maximum rainfall from the ensembles are listed above the panels.

the SA approach ranked first and third in RF_{max} and RI_{max} , respectively, in the correlation with QPESUMS data for the 10 cases (Fig. 12). However, the SA approach also produced relatively high root-mean-square errors (RMSE), ranking 22 and 13 in RF_{max} and RI_{max} , respectively. In contrast, the SM approach ranked 11th and 4th in the RMSE performance of RF_{max} and RI_{max} , respectively, whereas the correlation rankings are 5th and 20th, respectively. Note that the three ensembles should produce the same RMSE and correlation coefficient in average rainfall. Similar performance standings among the three ensembles can also be observed in Fig. 5. Such results suggest that the microphysical perturbation ensemble does not necessarily outperform most of the individual members in terms of peak rainfall. Nevertheless, the SA approach does show some promise in forecasting heavy rainfall from summer convection, considering that its high bias can be adjusted through regression analysis.

5. Conclusions

This study conducted microphysical perturbation experiments (MPE) to investigate the sensitivity of model results to cloud microphysical parameterization and the feasibility of

using a microphysical perturbation ensemble to forecast heavy rainfall due to summer-afternoon convection. We applied nine cloud microphysical parameterization schemes in the WRF model and eleven variations in process treatments within the multimoment (two for liquid- and three for ice-phase hydrometeors) NTU scheme to simulate 10 summer-afternoon heavy rain convections that occurred around the Taipei metropolis. Four additional simulations were conducted in a demonstration case to touch on the uncertainty in the collision efficiency by applying stochastic perturbations. We also ran a theta-perturbation ensemble, but the spread was small relative to that from perturbed microphysics.

Our simulations revealed large disagreements in the location and amplitude of peak rainfall among the MPE members. The range of spread in average rainfall, maximum rainfall, and maximum intensity relative to the observed heavy rain reached 57%–161%, 66%–161%, and 65%–149%, respectively, for the 10 simulated cases. Such discrepancies exist not only among different microphysical schemes but also among different process treatments within a single scheme (i.e., the NTU scheme). These process perturbation experiments show that convective heavy-rain formation is most sensitive to the following microphysical factors: fall speed parameterization, aerosol type, ice

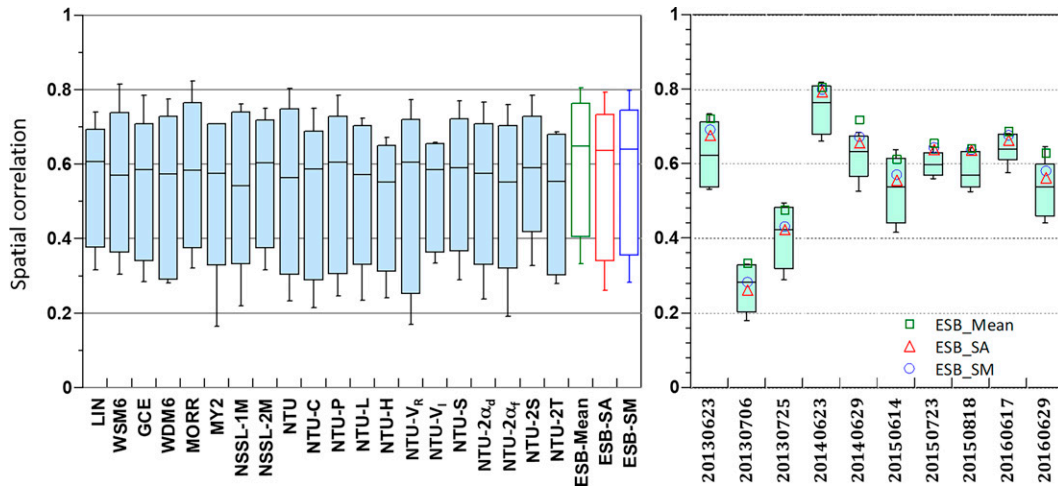


FIG. 11. Statistics of spatial correlation (against the QPESUMS data) from individual members for (left) all events and (right) from individual event for all members.

particle shape, and the spectral shape of the size distribution, at least within the context of the NTU scheme for these cases.

The large spread of results among the MPE members may provide a way to improve heavy-rain ensemble forecasting. Using the 10 cases, we demonstrated that the microphysical ensemble might produce a reasonable probability of occurrence for issuing a heavy-rain warning for specific locations. Such a probability forecast tends to be more successful for more organized convection, possibly because of their distinct thermodynamic or topographical forcing. Although a pinpoint precision for the location of heavy-rain warning might be difficult, we found that a fuzzy radius of about 8 km for the warning coverage can yield the best performance indices. With this fuzzy radius, the ensemble forecast may even obtain a threat

score for heavy-rainfall locations exceeding 0.6 for the more organized convection.

Besides the probability forecast for heavy rain locations, the MPE can also provide quantitative ensemble forecasts about heavy rainfall. As the simple ensemble mean tends to smear out the peak rainfall due to mismatch in locations, two spectral mapping methods were applied to map the peak values from individual members onto the spatial distribution resulting from the ensemble. We found that the spectral mapping ensembles can reasonably capture the rainfall pattern and amount, particularly for the more organized events. The spatial pattern from the ensembles correlated significantly better with the observations than those from individual members. For the 10 simulated cases, the “sort-all” mapping method

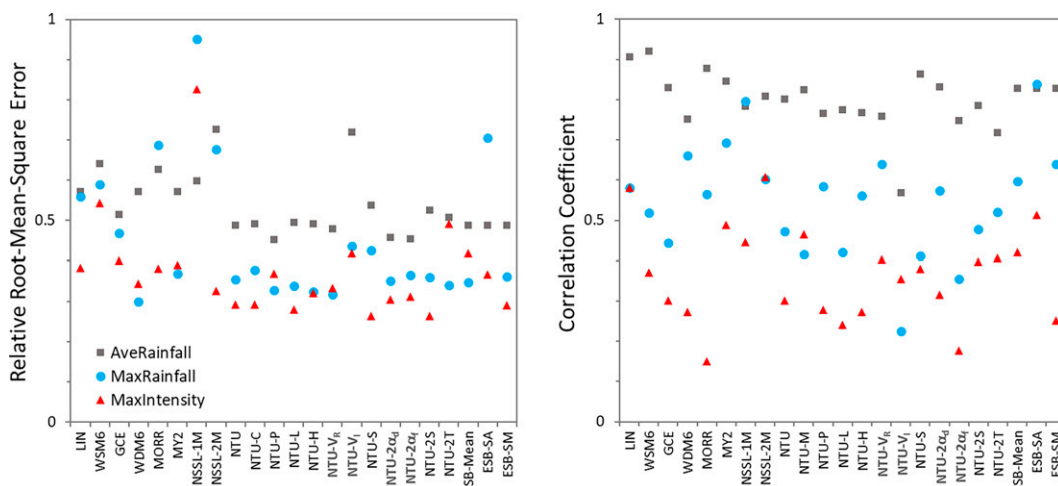


FIG. 12. Overall (10 case) performance in simulating average rainfall (gray squares), maximum accumulation (light-blue circles), and maximum intensity (red triangles) by the microphysical perturbation members and ensemble members evaluated against the QPESUMS data. (left) Relative root-mean-square error (RMSE) and (right) correlation coefficient. The relative RMSE is defined as the RMSE of rainfall indices normalized by the observed values.

produced rainfall amount well correlated with the observed rainfall, with correlation coefficients reaching 0.83, 0.84, and 0.51 for the average rainfall, maximum accumulation, and maximum intensity, respectively. Even though this method also produced substantial overestimations, the biases can be amended by a statistical adjustment such as linear regression. The other spectral mapping method (“sort within members”) caused smaller errors but also lower correlations. Nevertheless, more cases should be tested to gain sufficiently robust statistics before implementing such methods in operational applications.

The MPE conducted in this study may also be used for identifying the most sensitive perturbation members that should be considered for operational ensemble forecasts. For example, the selected microphysical parameters (the NTU members) are sufficient to create a spread close to that of MS members, which indicates that uncertainties in other unperturbed parameters are probably not as crucial. Such information can be used to reduce the size of MS perturbation members for future study. Furthermore, the essence of the ensemble approach is to apply perturbations to parameters that contain uncertainties but not correctable errors. With more case studies, one may also remove members (e.g., the member NTU-V) that frequently produce outliers and are identified as faulty or less physically realistic. After all, no perturbation is needed if the uncertainty is eliminated; therefore, improvements in microphysical parameterization from either physical or mathematical aspects are essential. On the other hand, the traditional hydrometeor-category-based microphysics schemes have inherent problems; therefore, microphysical schemes with novel approaches, such as those discussed in Morrison et al. (2020), might be considered new perturbation members.

Although a large spread in heavy rainfall simulation can result from the MPE, it remains to be clarified how such model spread compared with those from other perturbation methods, such as perturbations in initial and boundary conditions and different physics packages (cf. Du et al. 2018). This clarification is essential to selecting ensemble members for minimizing computational costs. Although this study focused on cloud microphysics, other uncertainties such as initial/boundary conditions or the inclusion of other physics schemes may influence our conclusion. Also, different model setups such as grid resolutions may further complicate the issue and are thus worthy of further investigation.

Acknowledgments. This study was supported through Grants MOST 105-2119-M-002-035, 106-2119-M-002-016, 07-2628-M-002 -016, 108-2119-M-002 -022, and 108-2111-M-002 -015 -MY3. We are grateful to the National Center for High-Performance Computing of National Applied Research Laboratories in Taiwan for providing computational and storage resources.

Data availability statement. The QPESUMS and rain gauge data for this study are available through <https://data.gov.tw/dataset/76629> and <https://data.gov.tw/dataset/6161>, respectively. The NTU scheme is available in the release of WRF version 4.3 or later through <https://github.com/wrf-model/WRF/releases>.

REFERENCES

- Akaeda, K., J. Reisner, and D. Parsons, 1995: The role of mesoscale and topographically induced circulations initiating a flash flood observed during the TAMEX project. *Mon. Wea. Rev.*, **123**, 1720–1739, [https://doi.org/10.1175/1520-0493\(1995\)123<1720:TROMAT>2.0.CO;2](https://doi.org/10.1175/1520-0493(1995)123<1720:TROMAT>2.0.CO;2).
- Andersson, T., M. Andersson, C. Jacobsson, and S. Nilsson, 1989: Thermodynamic indices for forecasting thunderstorms in southern Sweden. *Meteor. Mag.*, **118**, 141–146.
- Andreae, M. O., D. Rosenfeld, P. Artaxo, A. A. Costa, G. P. Frank, K. M. Longo, and M. A. F. Silva-Dias, 2004: Smoking rain clouds over the Amazon. *Science*, **303**, 1337–1342, <https://doi.org/10.1126/science.1092779>.
- Birch, C. E., D. J. Parker, J. H. Marsham, D. Copsey, and L. Garcia-Carreras, 2014: A seamless assessment of the role of convection in the water cycle of the West African Monsoon. *J. Geophys. Res. Atmos.*, **119**, 2890–2912, <https://doi.org/10.1002/2013JD020887>.
- Bougeault, P., and Coauthors, 2010: The THORPEX Interactive Grand Global Ensemble. *Bull. Amer. Meteor. Soc.*, **91**, 1059–1072, <https://doi.org/10.1175/2010BAMS2853.1>.
- Candille, G., S. Beauregard, and N. Gagnon, 2010: Bias correction and multiensemble in the NAEFS Context or how to get a “free calibration” through a multiensemble approach. *Mon. Wea. Rev.*, **138**, 4268–4281, <https://doi.org/10.1175/2010MWR3349.1>.
- Chang, P., and Coauthors, 2021: An operational multi-radar multi-sensor QPE system in Taiwan. *Bull. Amer. Meteor. Soc.*, **102**, E555–E577, <https://doi.org/10.1175/BAMS-D-20-0043.1>.
- Chen, C., K. Chung, S. Yang, L. Chen, P. Lin, and R. D. Torn, 2021: Sensitivity of forecast uncertainty to different microphysics schemes within a convection-allowing ensemble during SoWMEX-IOP8. *Mon. Wea. Rev.*, **149**, 4145–4166, <https://doi.org/10.1175/MWR-D-20-0366.1>.
- Chen, G. T. J., H. C. Chou, P. C. Liao, and J. S. Yang, 2009: Study on the warm season afternoon convection over northern and Central Taiwan (in Chinese with English abstract). *Atmos. Sci.*, **37**, 155–194.
- Chen, J.-P., and D. Lamb, 1994: Simulation of cloud microphysical and chemical processes using a multi-component framework. Part I: Description of the microphysical model. *J. Atmos. Sci.*, **51**, 2613–2630, [https://doi.org/10.1175/1520-0469\(1994\)051<2613:SOCMAC>2.0.CO;2](https://doi.org/10.1175/1520-0469(1994)051<2613:SOCMAC>2.0.CO;2).
- , and S. T. Liu, 2004: Physically-based two-moment bulk-water parameterization for warm cloud microphysics. *Quart. J. Roy. Meteor. Soc.*, **130**, 51–78, <https://doi.org/10.1256/qj.03.41>.
- , and T.-C. Tsai, 2016: Triple-moment modal parameterization for the adaptive growth habit of pristine ice crystals. *J. Atmos. Sci.*, **73**, 2105–2122, <https://doi.org/10.1175/JAS-D-15-0220.1>.
- Chen, S.-H., and W.-Y. Sun, 2002: A one-dimensional time dependent cloud model. *J. Meteor. Soc. Japan*, **80**, 99–118, <https://doi.org/10.2151/jmsj.80.99>.
- Chen, T.-C., S.-Y. Wang, and M.-C. Yen, 2007: Enhancement of afternoon thunderstorm activity by urbanization in a valley: Taipei. *J. Appl. Meteor. Climatol.*, **46**, 1324–1340, <https://doi.org/10.1175/JAM2526.1>.
- Du, J., G. DiMego, M. S. Tracton, and B. Zhou, 2003: CAS/JSC Working Group Numerical Experimentation: NCEP short-range ensemble forecasting (SREF) system: Multi-IC, multi-model and multiphysics approach. J. Cote, Ed., Research

- Activities in Atmospheric and Oceanic Modelling. WMO/TD Rep. 33, 1161 pp.
- , and Coauthors, 2018: Ensemble methods for meteorological predictions. NCEP Office Notes 493, 66 pp., <https://doi.org/10.7289/V5/QN-NCEP-493>.
- Duan, M., J. Ma, and P. Wang, 2012: Preliminary comparison of the CMA, ECMWF, NCEP, and JMA ensemble prediction systems. *Acta Meteor. Sin.*, **26**, 26–40, <https://doi.org/10.1007/s13351-012-0103-6>.
- Ebert, E. E., 2001: Ability of a poor man's ensemble to predict the probability and distribution of precipitation. *Mon. Wea. Rev.*, **129**, 2461–2480, [https://doi.org/10.1175/1520-0493\(2001\)129<2461:AOAPMS>2.0.CO;2](https://doi.org/10.1175/1520-0493(2001)129<2461:AOAPMS>2.0.CO;2).
- , 2008: Fuzzy verification of high-resolution gridded forecasts: A review and proposed framework. *Meteor. Appl.*, **15**, 51–64, <https://doi.org/10.1002/met.25>.
- Ehrendorfer, M., 1997: Predicting the uncertainty of numerical weather forecasts: A review. *Meteor. Z.*, **6**, 147–183, <https://doi.org/10.1127/metz/6/1997/147>.
- Fan, J., L. R. Leung, D. Rosenfeld, and P. J. DeMott, 2017: Effects of cloud condensation nuclei and ice nucleating particles on precipitation processes and supercooled liquid in mixed-phase orographic clouds. *Atmos. Chem. Phys.*, **17**, 1017–1035, <https://doi.org/10.5194/acp-17-1017-2017>.
- Fovell, R. G., K. L. Corbosiero, and H.-C. Kuo, 2009: Cloud microphysics impact on hurricane track as revealed in idealized experiments. *J. Atmos. Sci.*, **66**, 1764–1778, <https://doi.org/10.1175/2008JAS2874.1>.
- García-Díez, M., J. Fernández, and R. Vautard, 2015: An RCM multi-physics ensemble over Europe: Multi-variable evaluation to avoid error compensation. *Climate Dyn.*, **45**, 3141–3156, <https://doi.org/10.1007/s00382-015-2529-x>.
- Gastal, E. S. L., and M. M. Oliveira, 2017: Spectral remapping for image downscaling. *ACM Trans. Graph.*, **36**, 145, <https://doi.org/10.1145/3072959.3073670>.
- Gaudet, L. C., K. J. Sulia, T. C. Tsai, J.-P. Chen, and J. P. Blair, 2021: Assessment of a microphysical ensemble used to investigate the OWLeS IOP4 lake-effect storm. *J. Atmos. Sci.*, **78**, 1607–1628, <https://doi.org/10.1175/JAS-D-20-0045.1>.
- Georgii, H. W., and E. Kleijung, 1967: Relations between the chemical composition of atmospheric aerosol particles and the concentration of natural ice nuclei. *J. Rech. Atmos.*, **3**, 145–156.
- Gordon, J., and D. Albert, 2000: A comprehensive severe weather forecast checklist and reference guide. NOAA Tech. Rep. TSP-10, NWS Central Region, 46 pp.
- Grey, J. M., and J. A. Moorer, 1977: Perceptual evaluations of synthesized musical instrument tones. *J. Acoust. Soc. Amer.*, **62**, 454–462, <https://doi.org/10.1121/1.381508>.
- Haklander, A. J., and A. V. Delden, 2003: Thunderstorm predictors and their forecast skill for the Netherlands. *Atmos. Res.*, **67–68**, 273–299, [https://doi.org/10.1016/S0169-8095\(03\)00056-5](https://doi.org/10.1016/S0169-8095(03)00056-5).
- Harrington, J. Y., K. Sulia, and H. Morrison, 2013: A method for adaptive habit prediction in bulk microphysical models. Part I: Theoretical development. *J. Atmos. Sci.*, **70**, 349–364, <https://doi.org/10.1175/JAS-D-12-040.1>.
- Hohenegger, C., A. Walser, W. Langhans, and C. Schär, 2008: Cloud-resolving ensemble simulations of the August 2005 Alpine flood. *Quart. J. Roy. Meteor. Soc.*, **134**, 889–904, <https://doi.org/10.1002/qj.252>.
- Hong, S.-Y., and J.-O. J. Lim, 2006: The WRF single-moment 6-class microphysics scheme (WSM6). *J. Korean Meteor. Soc.*, **42**, 129–151.
- , Y. Noh, and J. Dudhia, 2006: A new vertical diffusion package with an explicit treatment of entrainment processes. *Mon. Wea. Rev.*, **134**, 2318–2341, <https://doi.org/10.1175/MWR3199.1>.
- Hoose, C., J. E. Kristjánsson, J.-P. Chen, and A. Hazra, 2010: A classical-theory-based parameterization of heterogeneous ice nucleation by mineral dust, soot, and biological particles in a global climate model. *J. Atmos. Sci.*, **67**, 2483–2503, <https://doi.org/10.1175/2010JAS3425.1>.
- Jankov, I., W. A. Gallus Jr., M. Segal, and S. E. Koch, 2007: Influence of initial conditions on the WRF-ARW model QPF response to physical parameterization changes. *Wea. Forecasting*, **22**, 501–519, <https://doi.org/10.1175/WAF998.1>.
- , and Coauthors, 2017: A performance comparison between multiphysics and stochastic approaches within a North American RAP ensemble. *Mon. Wea. Rev.*, **145**, 1161–1179, <https://doi.org/10.1175/MWR-D-16-0160.1>.
- Jefferson, G. J., 1963: A modified instability index. *Meteor. Mag.*, **92**, 92–96.
- Jimenez, P. A., J. Dudhia, J. F. Gonzalez-Rouco, J. Navarro, J. P. Montavez, and E. Garcia-Bustamante, 2012: A revised scheme for the WRF surface layer formulation. *Mon. Wea. Rev.*, **140**, 898–918, <https://doi.org/10.1175/MWR-D-11-00056.1>.
- Johnson, A., and Coauthors, 2014: Multiscale characteristics and evolution of perturbations for warm season convection-allowing precipitation forecasts: Dependence on background flow and method of perturbation. *Mon. Wea. Rev.*, **142**, 1053–1073, <https://doi.org/10.1175/MWR-D-13-00204.1>.
- Junker, N. W., and J. E. Hoke, 1990: An examination of nested grid model precipitation forecasts in the presence of moderate-to-strong low-level southerly inflow. *Wea. Forecasting*, **5**, 333–344, [https://doi.org/10.1175/1520-0434\(1990\)005<0333:AEONGM>2.0.CO;2](https://doi.org/10.1175/1520-0434(1990)005<0333:AEONGM>2.0.CO;2).
- Kain, J. S., 2004: The Kain-Fritsch convective parameterization: An update. *J. Appl. Meteor.*, **43**, 170–181, [https://doi.org/10.1175/1520-0450\(2004\)043<0170:TKCPAU>2.0.CO;2](https://doi.org/10.1175/1520-0450(2004)043<0170:TKCPAU>2.0.CO;2).
- Keita, S. A., E. Girard, J.-C. Raut, M. Leriche, J.-P. Blanchet, J. Pelon, T. Onishi, and A. Cirisan, 2020: A new parameterization of ice heterogeneous nucleation coupled to aerosol chemistry in WRF-Chem model version 3.5.1: Evaluation through ISDAC measurements. *Geosci. Model Dev.*, **13**, 5737–5755, <https://doi.org/10.5194/gmd-13-5737-2020>.
- Keresturi, E., Y. Wang, F. Meier, F. Weidle, C. Wittmann, and A. Atencia, 2019: Improving initial condition perturbations in a convection-permitting ensemble prediction system. *Quart. J. Roy. Meteor. Soc.*, **145**, 993–1012, <https://doi.org/10.1002/qj.3473>.
- Kuba, N., and Y. Fujiyoshi, 2006: Development of a cloud microphysical model and parameterizations to describe the effect of CCN on warm cloud. *Atmos. Chem. Phys.*, **6**, 2793–2810, <https://doi.org/10.5194/acp-6-2793-2006>.
- Kühnlein, C., C. Keil, G. C. Craig, and C. Gebhardt, 2014: The impact of downscaled initial condition perturbations on convective-scale ensemble forecasts of precipitation. *Quart. J. Roy. Meteor. Soc.*, **140**, 1552–1562, <https://doi.org/10.1002/qj.2238>.
- Lim, K.-S. S., and S.-Y. Hong, 2010: Development of an effective double-moment cloud microphysics scheme with prognostic cloud condensation nuclei (CCN) for weather and climate models. *Mon. Wea. Rev.*, **138**, 1587–1612, <https://doi.org/10.1175/2009MWR2968.1>.
- Lin, P.-F., P.-L. Chang, B. J.-D. Jou, J. W. Wilson, and R. D. Roberts, 2011: Warm season afternoon thunderstorm characteristics under weak synoptic-scale forcing over Taiwan

- island. *Wea. Forecasting*, **26**, 44–60, <https://doi.org/10.1175/2010WAF2222386.1>.
- , —, —, —, and —, 2012: Objective prediction of warm season afternoon thunderstorms in northern Taiwan using a fuzzy logic approach. *Wea. Forecasting*, **27**, 1178–1197, <https://doi.org/10.1175/WAF-D-11-00105.1>.
- Lorenz, E. N., 1969: The predictability of a flow which possesses many scales of motion. *Tellus*, **21**, 289–307, <https://doi.org/10.3402/tellusa.v21i3.10086>.
- Lynn, B. H., and Coauthors, 2001: Improved simulation of Florida summer convection using the PLACE land model and a 1.5-order turbulence parameterization coupled to the Penn State–NCAR mesoscale model. *Mon. Wea. Rev.*, **129**, 1441–1461, [https://doi.org/10.1175/1520-0493\(2001\)129<1441:ISOFSO>2.0.CO;2](https://doi.org/10.1175/1520-0493(2001)129<1441:ISOFSO>2.0.CO;2).
- Majumdar, S. J., and Coauthors, 2021: Multiscale forecasting of high-impact weather: Current status and future challenges. *Bull. Amer. Meteor. Soc.*, **102**, E635–E659, <https://doi.org/10.1175/BAMS-D-20-0111.1>.
- Mansell, E. R., C. L. Ziegler, and E. C. Bruning, 2010: Simulated electrification of a small thunderstorm with two-moment bulk microphysics. *J. Atmos. Sci.*, **67**, 171–194, <https://doi.org/10.1175/2009JAS2965.1>.
- Marinaki, A., M. Spiliotopoulos, and H. Michalopoulou, 2006: Evaluation of atmospheric instability indices in Greece. *Adv. Geosci.*, **7**, 131–135, <https://doi.org/10.5194/adgeo-7-131-2006>.
- Matsui, T., S. Q. Zhang, W.-K. Tao, S. Lang, C. Ichoku, and C. Peters-Lidard, 2018: Impact of radiation frequency, precipitation radiative forcing, and radiation column aggregation on convection-permitting West African Monsoon simulations. *Climate Dyn.*, **55**, 193–213, <https://doi.org/10.1007/s00382-018-4187-2>.
- Miao, J.-E., and M.-J. Yang, 2020: A modeling study of the severe afternoon thunderstorm event at Taipei on 14 June 2015: The roles of sea breeze, microphysics, and terrain. *J. Meteor. Soc. Japan*, **98**, 129–152, <https://doi.org/10.2151/jmsj.2020-008>.
- Milbrandt, J. A., and M. K. Yau, 2005a: A multimoment bulk microphysics parameterization. Part I: Analysis of the role of the spectral shape parameter. *J. Atmos. Sci.*, **62**, 3051–3064, <https://doi.org/10.1175/JAS3534.1>.
- , and —, 2005b: A multimoment bulk microphysics parameterization. Part II: A proposed three-moment closure and scheme description. *J. Atmos. Sci.*, **62**, 3065–3081, <https://doi.org/10.1175/JAS3535.1>.
- , H. Morrison, D. Dawson, and M. Paukert, 2021: A triple-moment representation of ice in the predicted particle properties (P3) microphysics scheme. *J. Atmos. Sci.*, **78**, 439–458, <https://doi.org/10.1175/JAS-D-20-0084.1>.
- Miller, R. C., 1972: Notes on analysis and severe storm forecasting procedures of the Airforce Global Weather Centre. AWS Tech. Rep. 200, Headquarters Air Weather Service, 106 pp.
- Mitchell, D. L., and A. J. Heymsfield, 2005: Refinements in the treatment of ice particle terminal velocities, highlighting aggregates. *J. Atmos. Sci.*, **62**, 1637–1644, <https://doi.org/10.1175/JAS3413.1>.
- Morrison, H., G. Thompson, and V. Tatarskii, 2009: Impact of cloud microphysics on the development of trailing stratiform precipitation in a simulated squall line: Comparison of one- and two-moment schemes. *Mon. Wea. Rev.*, **137**, 991–1007, <https://doi.org/10.1175/2008MWR2556.1>.
- , and Coauthors, 2020: Confronting the challenge of modeling cloud and precipitation microphysics. *J. Adv. Model. Earth Syst.*, **12**, e2019MS001689, <https://doi.org/10.1029/2019MS001689>.
- Nam, D. H., D. T. Mai, K. Udo, and A. Mano, 2014: Short-term flood inundation prediction using hydrologic-hydraulic models forced with downscaled rainfall from global NWP. *Hydrol. Processes*, **28**, 5844–5859, <https://doi.org/10.1002/hyp.10084>.
- Qiao, X., S. Wang, and J. Min, 2018: The impact of a stochastically perturbing microphysics scheme on an idealized supercell storm. *Mon. Wea. Rev.*, **146**, 95–118, <https://doi.org/10.1175/MWR-D-17-0064.1>.
- Rosenfeld, D., U. Lohmann, G. B. Raga, C. D. O'Dowd, M. Kulmala, S. Fuzzi, A. Reissell, and M. O. Andreae, 2008: Flood or drought: How do aerosols affect precipitation. *Science*, **321**, 1309–1313, <https://doi.org/10.1126/science.1160606>.
- Rotunno, R., and C. Snyder, 2008: A generalization of Lorenz's model for the predictability of flows with many scales of motion. *J. Atmos. Sci.*, **65**, 1063–1076, <https://doi.org/10.1175/2007JAS2449.1>.
- Sahlaoui, Z., S. Mordane, E. Wattrelot, and J. F. Mahfouf, 2020: Improving heavy rainfall forecasts by assimilating surface precipitation in the convective scale model AROME: A case study of the Mediterranean event of November 4, 2017. *Meteor. Appl.*, **27**, e1860, <https://doi.org/10.1002/met.1860>.
- Sanchez, J. L., E. G. Ortega, and J. L. Marcos, 2001: Construction and assessment of a logistic regression model applied to short-term forecasting in Leon (Spain). *Atmos. Res.*, **56**, 57–71, [https://doi.org/10.1016/S0169-8095\(00\)00089-2](https://doi.org/10.1016/S0169-8095(00)00089-2).
- Shahrbab, M., J. P. Walker, Q. J. Wang, A. Seed, and P. Steinle, 2016: An evaluation of numerical weather prediction based rainfall forecasts. *Hydrol. Sci. J.*, **61**, 2704–2717, <https://doi.org/10.1080/02626667.2016.1170131>.
- Showalter, A. K., 1953: A stability index for thunderstorm forecasting. *Bull. Amer. Meteor. Soc.*, **34**, 250–252, <https://doi.org/10.1175/1520-0477-34.6.250>.
- Sikder, S., and F. Hossain, 2016: Assessment of the weather research and forecasting model generalized parameterization schemes for advancement of precipitation forecasting in monsoon-driven river basins. *J. Adv. Model. Earth Syst.*, **8**, 1210–1228, <https://doi.org/10.1002/2016MS000678>.
- Skamarock, W. C., and Coauthors, 2008: A description of the Advanced Research WRF version 3. NCAR Tech. Note NCAR/TN-475+STR, 113 pp., <https://doi.org/10.5065/D68S4MVH>.
- Stanford, M. W., H. Morrison, A. Varble, J. Berner, W. Wu, G. McFarquhar, and J. A. Milbrandt, 2019: Sensitivity of simulated deep convection to a stochastic ice microphysics framework. *J. Adv. Model. Earth Syst.*, **11**, 3362–3389, <https://doi.org/10.1029/2019MS001730>.
- Tao, W.-K., J. Simpson, and M. McCumber, 1989: An ice–water saturation adjustment. *Mon. Wea. Rev.*, **117**, 231–235, [https://doi.org/10.1175/1520-0493\(1989\)117<0231:AIWSA>2.0.CO;2](https://doi.org/10.1175/1520-0493(1989)117<0231:AIWSA>2.0.CO;2).
- , J.-P. Chen, Z. Li, C. Wang, and C. Zhang, 2012: Impact of aerosols on convective clouds and precipitation. *Rev. Geophys.*, **50**, RG2001, <https://doi.org/10.1029/2011RG000369>.
- , D. Wu, S. Lang, J.-D. Chern, C. Peters-Lidard, A. Fridlind, and T. Matsui, 2016: High-resolution NU-WRF simulations of a deep convective-precipitation system during MC3E: Further improvements and comparisons between Goddard microphysics schemes and observations. *J. Geophys. Res. Atmos.*, **121**, 1278–1305, <https://doi.org/10.1002/2015JD023986>.
- Teller, A., and Z. Levin, 2006: The effects of aerosols on precipitation and dimensions of subtropical clouds: A sensitivity study using a numerical cloud model. *Atmos. Chem. Phys.*, **6**, 67–80, <https://doi.org/10.5194/acp-6-67-2006>.
- Tewari, M., and Coauthors, 2004: Implementation and verification of the unified Noah land surface model in the WRF model.

- 20th Conf. on Weather Analysis and Forecasting/16th Conf. on Numerical Weather Prediction, Seattle, WA, Amer. Meteor. Soc., 14.2, https://ams.confex.com/ams/84Annual/techprogram/paper_69061.htm.
- Toth, Z., and E. Kalnay, 1997: Ensemble forecasting at NCEP and the breeding method. *Mon. Wea. Rev.*, **125**, 3297–3319, [https://doi.org/10.1175/1520-0493\(1997\)125<3297:EFANAT>2.0.CO;2](https://doi.org/10.1175/1520-0493(1997)125<3297:EFANAT>2.0.CO;2).
- Tsai, T.-C., and J.-P. Chen, 2020: Multi-moment ice bulk microphysics scheme with consideration for particle shape and apparent density. Part I: Methodology and idealized simulation. *J. Atmos. Sci.*, **77**, 1821–1850, <https://doi.org/10.1175/JAS-D-19-0125.1>.
- Wang, H., T. Auligne, and H. Morrison, 2012: The impact of microphysics scheme complexity on the propagation of initial perturbations. *Mon. Wea. Rev.*, **140**, 2287–2296, <https://doi.org/10.1175/MWR-D-12-00005.1>.
- Wang, S., X. Qiao, and J. Min, 2020: Impact of stochastically perturbed terminal velocities on convective-scale ensemble forecasts of precipitation. *Adv. Meteor.*, **2020**, 4234361, <https://doi.org/10.1155/2020/4234361>.
- Weckwerth, T. M., 2000: The effect of small-scale moisture variability on thunderstorm initiation. *Mon. Wea. Rev.*, **128**, 4017–4030, [https://doi.org/10.1175/1520-0493\(2000\)129<4017:TEOSSM>2.0.CO;2](https://doi.org/10.1175/1520-0493(2000)129<4017:TEOSSM>2.0.CO;2).
- Whitby, K. T., 1978: The physical characteristics of sulfur aerosols. *Sulfur in the Atmosphere: Proceedings of the International Symposium*, R. B. Husar, J. P. Lodge Jr., and D. J. Moore, Eds., Pergamon, 135–159, <https://doi.org/10.1016/B978-0-08-022932-4.50018-5>.
- WMO, 2012: Guidelines on ensemble prediction systems and forecasting. WMO Doc. 1091, 32 pp.